Provenance analysis of the Yumen Basin and northern Qilian Shan: Implications for the pre-collisional paleogeography in the NE Tibetan plateau and eastern termination of Altyn Tagh fault

Feng Cheng, Carmala Garzione, Marc Jolivet, Weitao Wang, Jibao Dong, Fabiana Richter, Zhaojie Guo

Provenance analysis of the Yumen Basin and northern Qilian Shan: Implications for the pre-collisional paleogeography in the NE Tibetan plateau and eastern termination of Altyn Tagh fault

Feng Cheng, Carmala Garzione, Marc Jolivet, Weitao Wang, Jibao Dong, Fabiana Richter, Zhaojie Guo

PII: S1342-937X(18)30251-X
DOI: https://doi.org/10.1016/j.gr.2018.08.009
Reference: GR 2030

To appear in: *Gondwana Research*

Received date: 4 April 2018
Revised date: 22 July 2018
Accepted date: 18 August 2018

Please cite this article as: Feng Cheng, Carmala Garzione, Marc Jolivet, Weitao Wang, Jibao Dong, Fabiana Richter, Zhaojie Guo , Provenance analysis of the Yumen Basin and northern Qilian Shan: Implications for the pre-collisional paleogeography in the NE Tibetan plateau and eastern termination of Altyn Tagh fault. Gr (2018), https://doi.org/10.1016/j.gr.2018.08.009

Provenance analysis of the Yumen Basin and northern Qilian Shan: implications for the pre-collisional paleogeography in the NE Tibetan plateau and eastern termination of Altyn Tagh fault

Feng Cheng [1, 2, †], Carmala Garzione [1], Marc Jolivet [3], Weitao Wang [4], Jibao Dong [2], Fabiana Richter [1], Zhaojie Guo [5]

[1] Department of Earth and Environmental Sciences, University of Rochester, Rochester, NY 14627, USA

[2] State Key Laboratory of Loess and Quaternary Geology, Institute of Earth Environment, Chinese Academy of Sciences, Xi'an, 710075, China

[3] Laboratoire Géosciences Rennes, CNRS-UMR6118, Université Rennes 1, Observatoire des Sciences de l'Univers, Rennes, 35042, France

[4] State Key Laboratory of Earthquake Dynamics, Institute of Geology, China Earthquake Administration, Beijing, 100029, China

[5] Key Laboratory of Orogenic Belts and Crustal Evolution, Ministry of Education, School of Earth and Space Sciences, Peking University, Beijing, 100871, China

[†] Corresponding author: Feng Cheng (cfcf.chengfeng@gmail.com; fcheng5@ur.rochester.edu)

Abstract

Understanding the pre-collisional paleogeography in the NE Tibetan plateau provides insights into the growth mechanisms of the northern portion of the plateau in the Cenozoic. We conducted sandstone petrography analysis and determined U-Pb ages for detrital zircons from Cretaceous sandstone from the Yumen Basin and the northern Qilian Shan. Cretaceous strata in the northern Yumen Basin yield a unimodal age population at 290-240 Ma that indicates primary derivation from Bei Shan. Cretaceous strata in the westernmost Yumen Basin contain zircons of 2.6-2.2 Ga, 2.1-1.7 Ga, 1.4-0.7 Ga, 440-380 Ma and 300-230 Ma, suggesting source derivation from both the Qilian Shan and Bei Shan. Within the northern Qilian Shan, Cretaceous strata yield age populations of 2.8-2.3 Ga, 2.1-1.2 Ga, 480-380 Ma and ca. 270 Ma, indicating derivation from the Qilian Shan. Sandstone composition results show that a sample from the northern Qilian Shan contains more lithic fragments and plots in the recycled orogen field of the quartz-feldspar-lithics (QFL) diagram, while samples from Yumen Basin are more quartz-rich and plot close to the continental block field of the QFL diagram. This compositional difference corresponds to source variation, consistent with the detrital zircon record. Combined with existing sedimentology and low-temperature thermochronology datasets, we suggest the presence of Cretaceous topographic relief in the Bei Shan and Qilian Shan prior to India-Asia collision. Considering >300 km post-Cretaceous left-lateral offset along the Altyn Tagh Fault (ATF) and the consistently similar detrital zircon ages spectra of the samples from the Cretaceous to late Oligocene strata in the Yumen Basin, we infer the palaeogeography in the NE Tibetan plateau has been similar from the late Cretaceous to the late Oligocene with ATF termination in the western Yumen Basin instead of having been linked to strike-slip faults in the Alxa or other regions to the east since its initiation.

Keywords: Detrital zircon geochronology; Sandstone petrography; Northeastern Tibetan plateau; Altyn Tagh Fault; Cretaceous paleogeography

1 Introduction

It is widely acknowledged that the India-Asia collision in the early Cenozoic and the ongoing post-collisional convergence have driven the outward growth of the Tibetan plateau (Decelles et al., 2002; Dewey et al., 1988; England and Searle, 1986; Kapp et al., 2007b; Molnar and Tapponnier, 1975; Tapponnier et al., 2001; Yin and Harrison, 2000). As the pre-Himalayan orogenesis played a significant role in the topographic evolution of the modern Tibetan plateau, it is crucial to determine the pre-collisional paleogeography in the Tibetan plateau prior to the India-Asia collision.

In recent years, a growing body of evidence has suggested that the southern, southeastern, northern and eastern margins of Tibet (Fig.1), developed elevated topography prior to the collision (Cheng et al., 2016a; Cheng et al., 2015a; Ding et al., 2014; England and Searle, 1986; Enkelmann et al., 2006; Jolivet et al., 2001; Kapp et al., 2007a; Kapp et al., 2007b; Kapp et al., 2005; Leier et al., 2007; Li et al., 2017; Lippert et al., 2014; Murphy et al., 1997; Pullen et al., 2008; Roger et al., 2011; Tian et al., 2016a; Wu et al., 2016; Yang et al., 2017; Zhang et al., 2017) (Fig. 1). However, the late Mesozoic – early Cenozoic pre-collisional paleogeography of the northeastern Tibetan plateau is still poorly constrained, which may be attributed in part to the lack of detailed geologic information over the remote and often inaccessible Qilian Shan region (Fig. 1). Given that the present topography might be partly inherited from the Mesozoic geodynamic evolution, it is significant to determine the pre-collisional tectonics or paleogeography in the northeastern Tibetan plateau. Though few groups have conducted field investigations in the Yumen Basin and further inferred that the Qilian Shan to the south and Bei

Shan to the north might be the two major source areas of the late Mesozoic – early Cenozoic strata in the Yumen Basin (Peng, 2013; Wang et al., 2016c; Yang et al., 2011)(Fig. 1), the contribution of each source area as well as its variation through time have not been quantitatively estimated yet. Combined with existing datasets (including sedimentology, low-temperature thermochronology, etc.), a quantitative estimate of contribution of each source area contributes to a better understanding of the late Mesozoic – early Cenozoic paleogeography and growth of the northeastern Tibetan plateau.

Figure 1. (a) Digital topographic map of the Tibetan plateau. The timing of the pre-collisional deformation throughout the Tibetan plateau is based on previous studies (Cheng et al., 2016a; Cheng et al., 2015a; England and Searle, 1986; Enkelmann et al., 2006; George et al., 2001; Jolivet et al., 2001; Kapp et al., 2007a; Kapp et al., 2007b; Kapp et al., 2005; Leier et al., 2007; Li et al., 2017; Liu et al., 2013; Murphy et al., 1997; Pan et al., 2013; Pullen et al., 2008; Staisch et al., 2014; Tian et al., 2016a; Volkmer et al., 2007; Wang et al., 2017b; Yang et al., 2017; Zhang et al., 2017).

The modern left-lateral displacement along the Altyn Tagh Fault (ATF) marks the northern edge of the Tibetan plateau (Figs. 1 and 2a) and is considered to have accommodated about 300-500 km of intracontinental deformation in response to India-Asia collision and subsequent post-collisional convergence (Cheng et al., 2015a; Cheng et al., 2015b; Cheng et al., 2016b; Cowgill et al., 2003; Searle et al., 2011; Yin and Harrison, 2000; Yin et al., 2002; Zhang et al., 2014). However, the question of where the ATF terminated at its eastern tip during the Cenozoic (since its initiation) remains highly debated. Some workers suggest that the ATF terminated in the

Qilian Shan region since its Eocene or Miocene initiation (Burchfiel et al., 1989; Cheng et al., 2015b; Cowgill et al., 2003; Dupont-Nivet et al., 2004; Jolivet et al., 2001; Métivier et al., 1998; Wang et al., 2006; Wittlinger et al., 1998; Yin and Harrison, 2000; Yin et al., 2002) (Fig.1a). On the other hand, based on field investigation in the Yumen Basin, remote sensing image interpretation for the structures in the Hexi Corridor and Alxa block as well as the correlation between tectonic units and sutures in Bei Shan and the Inner Mongolia orogens, some studies argue that the ATF extended beyond the Qilian Shan since its initiation, linking with strike-slip faults in the Alxa block (East Mongolia), or even as far as the subduction system in the Sea of Okhotsk (Darby et al., 2005; Yue and Liou, 1999). If the Paleogene deformation along the ATF terminated in Qilian Shan, we would expect that the large amounts of sinistral displacement along the ATF since the India-Asia collision were largely transferred into Qilian Shan region and were accommodated by oblique slipping along the faults in the mountain ranges; otherwise such a large amount of deformation would be accommodated through left-lateral strike-slip displacement along the ATF and would be transferred to the region further to the east, out of Tibetan plateau. Given that these two different geometries proposed for the ATF at its eastern termination result in diverse understandings of the timing and mechanisms of crustal deformation in the northern Tibetan plateau, it is of primary importance to distinguish which geometry is accurate.

Detrital zircon geochronology has been developed as a valuable tool for unraveling source to sink relationships within a given area through time (Fedo et al., 2003; Thomas, 2011). In addition, great progress has been made in quantitative methods of unmixing detrital geochronology age distributions (Licht et al., 2016; Sundell and Saylor, 2017). In this study, we sampled five Cretaceous sandstone samples exposed in the Yumen Basin and northern Qilian

Shan (Figs. 2a and 3; Shan means “mountain” in Chinese), and determined the U-Pb ages of detrital zircons in these sandstones using laser-ablation inductively-coupled plasma mass spectrometry (LA-ICP-MS). To quantitatively determine mixing proportions of potential source contributions, a newly published software program DZmix (Sundell and Saylor, 2017) is used in this study. These results are interpreted in the context of sandstone petrologic results, previously published detrital zircon geochronology, published paleocurrent data in the Yumen Basin, as well as existing low-temperature thermochronology data in the NE Tibetan plateau for a better understanding of the Cretaceous-Cenozoic paleogeography of the NE Tibetan plateau. Moreover, detrital zircon geochronology is also a powerful means of resolving the displacement history of potentially displaced terranes (Cheng et al., 2016b; Gehrels, 2014). Outcropped near the highly debated eastern end of the ATF, the Cretaceous to Cenozoic strata in the Yumen Basin provide a good proxy for examining the source variation through time due to the potential sinistral slip motion of the ATF since its Eocene or Miocene initiation. In the context of the abovementioned published datasets, we compare age distributions of detrital zircon from the Cretaceous to Cenozoic strata in the Yumen Basin to estimate the potential source variation and further define the geometry of the eastern termination of the ATF.

Figure 2. (a) Geological map of the northeastern Tibetan plateau and locations of the detrital zircons samples from the Yumen Basin and the Qilian Shan. Four modern fluvial sand samples (BS2, BS3, QL1 and QL2) are from our previous work (Wang et al., 2016c). The ages presented are from previous geochronology studies (Bovet et al., 2009; Chen et al., 2014b; Chen et al., 2012; Duan et al., 2015; Gehrels et al., 2003b; Gong et al., 2017; Lu et al., 2008; Song et al., 2013; Song et al., 2009; Tseng et al., 2007; Tung et al., 2007; Tung et al., 2016; Wang et al.,

2017a; Wang et al., 2016a; Wei and Song, 2008; Xia and Song, 2010; Xu et al., 2015; Yang et al., 2009; Yu et al., 2015; Zeng et al., 2016; Zhang et al., 2007a; Zheng et al., 2017b). (b) and (c) are two cross-sections through the Yumen Basin, showing the distribution of the Cretaceous and Cenozoic strata in this region, modified from Dai et al. (2005). NQF, North Qilian Fault; NKF, northern marginal fault of the Kuantan Shan-Longshou Shan; SKF, southern marginal fault of the Kuantan Shan.

Figure 3. Geological map of the Yumen Basin and northern Qilian Shan. The black dash line refers to the extent of the northern Qilian Shan, adapted from previous studies (Bovet et al., 2009; Gehrels et al., 2003b).

2 Regional geology

2.1 Qilian Shan, Yumen Basin and Altyn Tagh Fault

The Qilian Shan marks the northeastern margin of the Tibetan plateau, occupying a transition zone between the high elevation plateau and the adjacent low-elevation cratons (Lease, 2014; Meyer et al., 1998; Tapponnier et al., 1990) (Fig. 1). The Qilian Shan contains massive NW-SE striking ranges that grow on folds, thrusts or strike-slip faults accommodating the northward motion of the Tibetan plateau (Allen et al., 2017; Meyer et al., 1998; Yin and Harrison, 2000; Zuza et al., 2016). Based on field investigation in the Qaidam Basin and Yumen Basin, low temperature thermochronology from the basement rocks in the northern Qilian Shan or from the Cenozoic sedimentary rocks in the Yumen Basin, and provenance analysis of the Cenozoic strata in the Yumen Basin and northern Qilian Shan, some studies have argued that

crustal shortening and surface uplift began in the southern Qilian Shan during the Paleogene (Wang et al., 2017c; Yin et al., 2008; Zhuang et al., 2011) and later propagated northward into the central and northern Qilian Shan (Bovet et al., 2009; Lease, 2014; Métivier et al., 1998; Meyer et al., 1998; Wang et al., 2016b; Zheng et al., 2010; Zhuang et al., 2011). However, the overall data coverage of dataset is still sparse, which is partly attributed to the lack of detailed geologic information over the remote and often inaccessible mountain ranges in the Qilian Shan. In this study, we follow the previous definition of the northern Qilian Shan (Bovet et al., 2009; Gehrels et al., 2003b). The extent of the northern Qilian Shan is labelled in Figure 3. The Qilian Shan is bordered by the Hexi Corridor to the north and truncated by the lithosphere-scale, sinistral strike-slip ATF to the west (Figs. 1 and 2). Left-lateral displacement along the ATF has accommodated hundreds of kilometers of the post-collisional convergence between the India and Asia, but the estimates of its total offset generally vary between ca. 300 km to ca. 500 km (Chen et al., 2002; Cheng et al., 2015a; Cheng et al., 2015b; Cheng et al., 2016b; Cowgill et al., 2003; Ritts and Biffi, 2000; Searle et al., 2011; Yin et al., 2002).

A series of transpressional faults developed in the Hexi Corridor in response to the northward propagation of the Qilian Shan, separating several sub-basins (Wang et al., 2016b). The Yumen Basin, in the transition zone between the northern Qilian Shan and the Bei Shan, is the westernmost sub-basin of the Hexi Corridor (Fig. 2a). The middle Eocene to Quaternary strata (including the Huoshaogou, Baiyanghe, Sulehe, Yumen, and Jiuquan formations, from the oldest to the youngest) of the Yumen Basin are well-exposed (Peng, 2013; Wang et al., 2016b), composed of alluvial to marginal lacustrine deposits (Dai et al., 2005; Wang et al., 2016c; Wang et al., 2016d; Yang et al., 2011) (Figs. 2-4). Those Cenozoic strata unconformably overlie Lower Cretaceous strata (Figs. 4 and 5) that are widespread along the northern Qilian Shan and

in the Yumen Basin (Figs. 2a and 3). In the northern Qilian Shan, the Lower Cretaceous strata mainly consist of thick beds of massive red conglomerate and coarse sandstone associated with high energy proximal fluvial and alluvial fan depositional settings (Peng, 2013) (Fig. 4). In the Yumen Basin, especially in its central and northern parts, the Lower Cretaceous strata are mainly composed of thin beds of greenish grey claystone and siltstone intercalated with thin to thick beds of brownish grey massive sandstone and conglomerate, corresponding to lacustrine facies deposits (Peng, 2013).

Figure 4. Lithostratigraphy of the five studied sections. (a) Caogou section (Wang et al., 2016b), (b) Huoshaogou section (Dai et al., 2005), (c) northern Qilian Shan section, (d) Jingtieshan section and (e) Hongliuxia section (Peng, 2013). D, S, F, M, C, and G represent claystone, siltstone, fine-grained sandstone, medium-grained sandstone, coarse-grained sandstone, and conglomerate, respectively. Magnetostratigraphy of the Caogou and Huoshaogou sections and their correlation with GPTS12 (Hilgen et al., 2012) are from Dai et al. (2005); Wang et al. (2016b), respectively. These five sections are measured from both this study and previous work (Dai et al., 2005; Peng, 2013; Wang et al., 2016b). The paleocurrent measurements are from previous work (Dai et al., 2005; Peng, 2013; Wang et al., 2016c). FZ1-FZ5, and FZ7 are Cenozoic detrital zircon samples from our previous work (Wang et al., 2016c).

Figure 5. Photographs of the Lower Cretaceous strata in the Yumen Basin and Qilian Shan. (a) shows a Cretaceous NNE-SSW striking normal fault in the northern Qilian Shan. Note that the Lower Cretaceous strata becomes coarser towards the normal fault, corresponding with syntectonic deposition. (b) shows the unconformity between the Lower Cretaceous strata and the

overlying Eocene Huoshangou Fm., Huoshaogou section (c) represents a grey white tabular sandstone interbedded with thin purple and greenish claystone beds in the Lower Cretaceous strata, Huoshaogou section, corresponding to distal lacustrine facies deposits. (d) shows the angular unconformity between the Lower Cretaceous strata and the overlying Oligocene Baiyanghe Fm., Caogou section. (e) represents Lower Cretaceous strata of the Caoguo section, showing thickly bedded sandstone intercalated with thin lenses of small pebbles, corresponding to braided river deposits. (f) represents the unconformity between Lower Cretaceous strata and the overlying Oligocene Baiyanghe Fm., Hongliuxia section. (g) displays early Cretaceous basalt (ca. 116-106 Ma, determined by Yang et al. (2001) and Peng (2013)), (h) represents purple-red thickly bedded conglomerate, within northern Qilian Shan section, pertaining to proximal deposits. (i) shows a purple massive sandstone intercalation in a thick bedded Lower Cretaceous conglomerate, northern Qilian Shan section. (j) represents a thickly bedded conglomerate intercalated with thinly bedded sandstone in the Lower Cretaceous strata, Jingtieshan section, pertaining to proximal deposits.

2.2 Early Cretaceous tectonics in the Yumen Basin, Bei Shan and northern Qilian Shan

Based on the field investigations, previous studies have determined the depositional environment of Lower Cretaceous strata outcropped in the western Yumen Basin and have inferred an extensional tectonic setting during the early Cretaceous (Peng, 2013; Yang et al., 2011). Field geological surveys, combined with $^{40}Ar/^{39}Ar$ thermochronology and zircon U-Pb geochronology dating, have identified a series of ca. 116-106 Ma mafic volcanic rocks in the

western Yumen Basin that has been interpreted as a consequence of extensional tectonics during the early Cretaceous (Peng, 2013; Yang et al., 2001). In addition, seismic reflection surveys in the Yumen Basin shows early Cretaceous growth strata deposited in the hanging wall of a series of NNE-SSW striking normal faults, again indicating an extensional setting during the early Cretaceous (Chen et al., 2014a). Evidenced from the low-temperature thermochronology, the basement rocks of Bei Shan experienced an episode of relatively rapid cooling during the early Cretaceous, indicative of rapid basement exhumation (Gillespie et al., 2017; Tian et al., 2016b). This early Cretaceous tectonic reactivation might either correspond to the Lhasa/Eurasia collision and subsequent slab break-off, or link with the collision along Mongol-Okhosk Orogeny and subsequent collapse (Gillespie et al., 2017; Jolivet et al., 2013b; Jolivet et al., 2010). Due to the lack of the geological information in the remote Qilian Shan region, the early Cretaceous tectonic setting in the Qilian Shan is not well constrained. Based on apatite fission track analysis, previous work has demonstrated Cretaceous cooling and exhumation of the northern Qilian Shan (George et al., 2001; Jolivet et al., 2001; Pan et al., 2013). Our field investigation observed a NNE-SSW trending normal fault in the northern Qilian Shan (Fig. 5a), likely indicative of an extensional setting in the northern Qilian Shan during the early Cretaceous. Further effort should be made to unravel the tectonic setting in the Bei Shan and Qilian Shan regions.

2.3 Stratigraphy and sediment characteristics of the studied sections

Three of our studied sections are located in the Yumen Basin, namely the Caogou, Huoshaogou and Hongliuxia sections (Figs. 2-4). The Jingtieshan and northern Qilian Shan sections are located in the northern Qilian Shan (Figs. 2-4). In the Caogou and Huoshaogou

sections, the Lower Cretaceous strata underlie unconformably the late Eocene to Oligocene Huoshaogou Fm. (Fig. 5b, 5d). The Lower Cretaceous strata mainly consist of thinly bedded of greenish grey laminated claystone and siltstone interbedded with thin to medium tabular beds of grey massive sandstone, corresponding to distal lacustrine facies deposits (Peng, 2013) (Fig. 5c, 5e). Paleocurrent measurements indicate south-directed unidirectional paleoflows (Dai et al., 2005). In the Hongliuxia section, the Lower Cretaceous strata were unconformably overlain by the Oligocene Baiyanghe Fm. strata (Fig. 5f). The Lower Cretaceous deposits are mainly composed of thin beds of greenish grey claystone and sandy claystone interbedded with greenish grey sandstone, sandy claystone and thick beds of sandstone, corresponding to a distal alluvial plain to proximal lacustrine environments (Peng, 2013)(Fig. 5f-5g). Clast imbrications in this section suggest multiple paleocurrent directions (e.g. NNW-directed and south-directed) (Peng, 2013). In the Northern Qilian Shan and Jingtieshan sections, the Lower Cretaceous strata unconformably underlie the Oligocene Baiyanghe Fm., and unconformably overlie the basement rocks of the northern Qilian Shan. The Cretaceous strata are mainly composed of thick beds of purple to red conglomerate intercalated with thin to medium bedded tabular sandstone (Fig. 5h-j). The poorly-rounded and poorly-sorted conglomerates indicate that material has not been transported very far, pertaining to proximal deposits (Fig. 5h-5j). Detailed sedimentological descriptions of the sampled Cretaceous sections can also be found in Peng (2013).

Figure 6. (a)-(e) Cross-polarized light photomicrograph of five Cretaceous samples. (f)-(g) are ternary diagrams (Qt-F-L plot and Qm-F-Lt plot) displaying the relative abundance of framework grains in sandstone from the Cretaceous strata in the Yumen Basin and northern Qilian Shan. The provenance fields follow the method of Dickinson et al. (1983). Sample NQL-

K, from the northern Qilian Shan, has highest content of lithic rock fragment and plots in the "recycled orogen" field in both the QtFL and QmFLt diagrams. Sample HLX-K, from the southwestern Yumen Basin has second-highest content of lithic rock fragment and plots in the "recycled orogen" field in both the QtFL and QmFLt diagrams. Samples CG-K and HSG-K, from the northern Yumen Basin, have lowest content of lithic fragments and plot near the boundary between the "continental block" and "recycled orogen" fields in both the QtFL and QmFLt diagrams. We interpret that the sources for the strata in the Yumen Basin and Qilian Shan are different during the Cretaceous. Qt: total quartz, Qm: monocrystalline quartz, F, feldspar, L: lithic rock fragments, Lt: total lithics (lithic rock fragments + polycrystalline quartz).

3 Approach and Methods

3.1 Sandstone petrography

Five Cretaceous sandstone samples, namely CG-K, HSG-K, HLX-K, NQL-K and JST-K, were collected from the Yumen Basin and northern Qilian Shan for petrographic analysis. We prepared standard thin sections and stained the thin sections to identify potassium feldspar. We used cross-polarization microscope to observe the petrographic features, including mineral composition, grain size, sorting and roundness. Cross-polarized light photomicrographs of these five samples are shown in Fig. 6a-6e. Modal compositions were then determined by utilizing the modified Gazzi-Dickinson point-counting method (Ingersoll et al., 1984). According to the method of Dickinson and Suczek (1979), sample JTS-K containing more than 25% of matrix or cement has been excluded from consideration (Fig. 6e). A minimum of 400 points were counted per sample. Raw point-counting data are summarized in the supplementary

material. Samples were classified and plotted on the ternary diagrams (Fig. 6f-6g) using the scheme outlined in (Dickinson et al., 1983). We follow the mineral abbreviation of Dickinson and Suczek (1979) to better describe our results: Qt for total quartz, Qm for monocrystalline quartz, F for feldspar, L for lithic rock fragments, and Lt for total lithic grains including polycrystalline quartz.

3.2 Detrital zircon geochronology

Combined with sedimentology and low-temperature thermochronology datasets, detrital zircon U-Pb geochronology has been widely used to understand the paleogeography of a region by reconstructing the source of sediment in ancient sedimentary systems (Gehrels, 2014; Gehrels and Pecha, 2014). In this study, we collected five sandstone samples (about 5kg each) from Cretaceous outcrops and extracted zircon grains following the standard procedures outlined in Li et al. (2004). This work was carried out at the Chengxin Geology Service Co. Ltd., Langfang, China. In order to avoid sampling bias, zircon crystals (generally >200 grains) were mounted in epoxy resin without handpicking, together with fragments or loose grains of Sri Lanka, FC-1, and R33 zircon crystals for use as standards. Zircon crystals were then polished to obtain a smooth internal surface.

Zircon U-Pb dating was conducted using laser ablation inductively coupled plasma mass spectrometry (LA-ICPMS) at the Arizona LaserChron Center (Gehrels and Pecha, 2014; Gehrels et al., 2006; Gehrels et al., 2008). All five samples were ablated using a 30 μm laser beam diameter. Detailed methods for analysis on the laser-coupled Thermo Element 2 single-collector ICP-MS were previously described by Pullen et al. (2014).

Common Pb corrections were performed based on the measured $^{206}Pb/^{204}Pb$ and the assumed composition of common Pb from Stacey and Kramers (1975). Sri Lanka and FC-1 zircon

standards were used to correct for isotope fractionation, and the R33 zircon standard was treated as an unknown and used to monitor the fractionation correction. Reported uncertainties include measurement errors at the 1σ level. Analyses with >10% uncertainty (1σ) in $^{206}Pb/^{238}U$ age are not included. Analyses with >10% uncertainty (1σ) in $^{206}Pb/^{207}Pb$ age are not included, unless $^{206}Pb/^{238}U$ age is <400 Ma. Best age was determined from $^{206}Pb/^{238}U$ age for analyses with $^{206}Pb/^{238}U$ age younger than 900 Ma and from $^{206}Pb/^{207}Pb$ age for analyses with $^{206}Pb/^{238}U$ age older than 900 Ma. U concentration and U/Th ratio were calibrated relative to Sri Lanka zircon standard and are accurate to ~20%. Using the routines in Isoplot 3.7 relative age-probability diagrams (Ludwig, 2008). Isotopic ages with errors and related raw data are presented in the supplementary material.

In order to extract mixing proportions of source rocks contributions, a newly published MATLAB-based inverse Monte Carlo method was used (Sundell and Saylor, 2017). By randomly constructing known source age distribution for comparison to individual mixed samples, this new technique can be used to constrain forward optimization routines to find a best model fit. We then determine mixing proportions of source rock contributions for each tested mixed sample. The details about this inverse Monte Carlo method are available in Sundell and Saylor (2017).

4 Results

4.1 Sandstone petrographic results

Samples CG-K and HSG-K were collected in the Caogou and Huoshaogou sections, respectively (Figs. 2 and 3), from fine- to medium-grained sandstones. Both samples are well to moderately sorted and characterized by subangular to subrounded grains (Fig. 6a-6b). The modal

compositions of sample HSG-K are Qt: F: L= 68:22:10, plotting near the boundary between "transitional continental" field and "recycled orogen" field (Fig. 6f) in the QtFL diagram and Qm: F: Lt=59:22:19, plotting near the boundary between "transitional continental" field and "quartzose recycled" field in the QmFLt diagram (Fig. 6g). Modal compositions for sample HSG-K are Qt: F: L= 58:35:7, plotting near the boundary between "transitional continental" field and "recycled orogen" field in the QtFL diagram (Fig. 6f) and Qm: F: Lt=47:35:18, plotting near the boundary between the "transitional continental" field and "mixed" field in the QmFLt diagram (Fig. 6g).

Sample HLX-K was collected in the Hongliuxia section (Figs. 2 and 3), from fine- to medium-grained sandstone. Sample HLX-K is characterized by moderately sorted and subangular to subrounded grains (Fig. 6c). Modal compositions for sample HLX-K are Qt: F: L= 62:14:24 and Qm: F: Lt=39:14:48, plotting in the "recycled orogen" field in the QtFL diagram (Fig. 5f) and "quartzose recycled" field in the QmFLt diagram, respectively (Fig. 6g).

Samples NQL-K and JTS-K were collected in the northern Qilian Shan (Figs. 2 and 3), from coarse- to medium-grained sandstones. Both samples are characterized by very poorly to poorly sorted and characterized by very angular to angular grains (Fig. 6d-6e). Modal compositions for sample NQL-K are Qt: F: L= 47:17:36 and Qm: F: Lt=30:17:53, plotting in the "recycled orogen" field in the QtFL diagram (Fig. 6f) and near the boundary between "quartzose recycled" field and "mixed" field in the QmFLt diagram (Fig. 6g), respectively.

4.2 Detrital zircon geochronology results

U-Pb concordia diagrams for zircon grains of each sample are shown in Figure 7a-7e. Previous studies have suggested that the zircon grains of magmatic origin normally have high

Th/U radios (>0.1), while the zircon grains of metamorphic origin have low Th/U radios (<0.1)(Belousova et al., 2002; Hoskin and Black, 2000). Analyzed zircon age vs. Th/U ratios are shown in Figure 7f, indicating the predominant magmatic origin of all the analyzed zircons. Zircon U-Pb age cumulative probability distribution for each sample are shown in Figure 8. Following our previous criteria (Cheng et al., 2016a), age peaks are considered major when including at least 20% of the total number of data spread over less than 250 Ma, whereas a minor peak refers to populations representing less than 20% of the total number of data distributed over more than 300 Ma.

Figure 7. (a)-(e) U-Pb concordia diagrams for zircon grains of each sample. The diagrams were constructed from the software provided by the Arizona LaserChron Center Web site (http://www.laserchron.org). (f) Age of analyzed zircons vs. Th/U ratios.

The zircon grains in sample CG-K are large (80-200 μm) with euhedral to abraded shapes. The Th/U ratios vary from 0.10 to 1.67, with four exceptions of 0.02 (412 Ma), 0.03 (424 Ma), 0.08 (258 Ma) and 0.09 (431 Ma), confirming the predominant magmatic origin of the zircons (Belousova et al., 2002; Hoskin and Black, 2000). Among the 110 analyzed zircons, 106 U-Pb ages with discordance degree <10% were obtained. The U-Pb ages range from 1957 Ma to 221 Ma with a single peak at 278-240 Ma (Fig. 8i). The zircon crystals in sample HSG-K show euhedral to abraded shapes, with an average size ranging between 25 μm and 150 μm. The Th/U ratios vary from 0.15 to 1.71, with only one exception of 0.05 (247 Ma), confirming a magmatic source. Among the 110 analyzed crystals, 109 effective ages were obtained. The U-Pb ages vary from 1924 Ma to 229 Ma, with a unimodal age peak at 288-242 Ma (Fig. 8j).

Figure 8. (a)-(s) Zircon U-Pb age cumulative probability distribution for each sample constructed with the program from the Arizona LaserChron Center Web site (http://www.laserchron.org). BS2 and BS3 are modern river samples from Bei Shan, from our previous work (Wang et al., 2016c). QL1 and QL2 are modern river samples from Qilian Shan, from our previous work (Wang et al., 2016c). Zircon U-Pb age cumulative probability distributions of these modern river samples are used to characterize the age of granitoid plutons in the Qilian Shan and Bei Shan (Wang et al., 2016c). FZ1, FZ2 and FZ4-FZ7 are Cenozoic samples obtained from the Caogou section, from our previous work (Wang et al., 2016c). CG-K, HSG-K, HLX-K, NQL-K and JTS-K are new samples collected from the Cretaceous strata in the Caogou, Huoshangou, Hongliuxia, Northern Qilian Shan, and Jingtieshan sections, respectively. Locations of these samples are shown in Figs. 2 and 3. Note the consistent age-distribution from Cretaceous to early Miocene samples (g-j). The color change from green to orange in the vertical shaded areas represents source variation. (t) Multidimensional scaling map (Vermeesch, 2013), showing the distinct signature of Bei Shan and Qilian Shan source regions. The multi-dimensional scaling (MDS) map uses the Kolmogorov–Smirnov (KS) statistic for detrital zircon U–Pb datasets (Stevens et al., 2013; Vermeesch, 2013). Axes are in dimensionless "K–S units" ($0 < KS < 1$), showing distance between samples. Solid lines and dashed lines connect samples with their "closest" and "second closest" neighbors, respectively. Blue solid circles represent detrital zircon data from the Cretaceous samples in this study. Pink solid circles represent detrital zircon data from the Cenozoic samples from Wang et al. (2016c). Green solid circles represent detrital zircon data from modern river samples in Bei Shan, while yellow solid circles represent detrital zircon data from modern river samples in the Qilian Shan. These four modern rivers

detrital zircon data are from Wang et al. (2016c). Note that zircon age distributions from samples FZ1, FZ2, HSG-K and CG-K are statistically similar with those of modern river samples from the Bei Shan region (samples BS2 and BS3), whereas zircon age distributions from samples FZ4, FZ5, FZ6, FZ7, NQL-K, JTS-K and HLX-K are statistically similar with those of modern river samples sourced from the Qilian Shan region (samples QL1 and QL2).

In sample HLX-K, the zircon grains show euhedral to abraded shapes and an average size of 50 μm to 250 μm. The Th/U ratios vary from 0.11 to 2.91, with two exceptions of 0.03 (360 Ma) and 0.04 (1034 Ma), indicative of a largely magmatic origin (Belousova et al., 2002; Hoskin and Black, 2000). Among the 110 analyzed zircons, 101 ages were obtained with discordance degree <10%. Five major age populations dominate with peaks at ca. 2580-2200 Ma, 2058-1710 Ma, 1380-780 Ma, 440-380 Ma, 280-230 Ma (Fig. 8o).

The zircon grains from sample NQL-K show euhedral to abraded shapes, with an average size ranging between 25 μm to 250 μm. The Th/U ratios range from 0.10 to 1.59, with one exception of 0.03 (388 Ma), confirming a magmatic source (Belousova et al., 2002; Hoskin and Black, 2000). One-hundred and ten crystals were analyzed, and 100 ages have discordance degree <10%. The U-Pb ages range from 2899 Ma to 231 Ma, and can be divided into three populations with one major peak at ca. 440 Ma and two minor peaks at 1920-1600 Ma and ca. 275 Ma, respectively (Fig. 8p).

In sample JTS-K, the zircon crystals are smaller (20-100 μm) compared with the grains in the previous samples and again show euhedral to abraded shapes. The Th/U ratios range from 0.10 to 5.84, with six exceptions of $1.9*10^{-5}$ (1331 Ma), 0.02 (2705 Ma), 0.03 (233 Ma), 0.06 (392 Ma), 0.09 (991 Ma) and 0.09 (1921 Ma), suggesting the predominant magmatic origin of

the zircons (Belousova et al., 2002; Hoskin and Black, 2000). In total, 110 crystals were analyzed, and 97 ages have discordance degree <10%. The U-Pb ages range from 2912 Ma to 155 Ma with four distinct peaks at ca. 2740-2280 Ma, 2050-1180 Ma, 435 Ma and 278 Ma (Fig. 8q).

5 Discussion

5.1 Provenance analysis

By systemically comparing the detrital zircon dataset obtained from the Cretaceous samples in the Yumen Basin and northern Qilian Shan with known ages of the potential source terranes, we can determine the source to sink relationship between the Yumen Basin and the surrounding mountain belts. Based on the detrital zircon analysis of modern fluvial sand samples together with the U–Pb geochronology of basement rocks, previous studies have revealed the distinct U-Pb age signature of the northern Qilian Shan and Bei Shan regions (Bovet et al., 2009; Chen et al., 2014b; Chen et al., 2012; Cheng et al., 2017; Duan et al., 2015; Gehrels et al., 2003b; Gong et al., 2017; Lu et al., 2008; Song et al., 2013; Song et al., 2009; Tseng et al., 2007; Tung et al., 2007; Tung et al., 2016; Wang et al., 2017a; Wang et al., 2016a; Wei and Song, 2008; Xia and Song, 2010; Xu et al., 2015; Yang et al., 2009; Yu et al., 2015; Zeng et al., 2016; Zhang et al., 2007a; Zheng et al., 2017b) (Fig. 8a-8b, 8k-8n, 8r-8s). The northern Qilian Shan basement mainly consists of Archean-middle Proterozoic orthogeisses/granitoid plutons with zircon U-Pb ages spanning from 2.6 Ga to 1.0 Ga, late Proterozoic intrusions with zircon U-Pb ages between 1.0 Ga and 700 Ma, early Paleozoic granitoid plutons with zircon U-Pb ages ranging from 550 Ma to 420 Ma and a few Permian to Triassic igneous rocks with zircon U-Pb ages ranging between 280 Ma and 200 Ma (Fig. 8a-8b, 8r-8s). Some work suggests that the Precambrian

zircons in the northern Qilian Shan might have been recycled from the underthrust basement of the Alxa block (Gehrels et al., 2003a, b). With regards to the basement rocks of the Bei Shan, late Paleozoic and early Mesozoic granite plutons widely crop out, with zircon U-Pb ages ranging from 310 Ma to 230 Ma (Fig. 8k-8n).

To understand the similarities/dissimilarities between individual samples and basement of Bei Shan and Qilian Shan regions, we adapt the multidimensional scaling (MDS) map that was developed to create a spatial visualization to determine the misfit between age distributions using the Kolmogorov–Smirnov (KS) test as the dissimilarity measure (Vermeesch, 2013). As shown in Figure 8t, zircon age distributions of Lower Cretaceous samples from the northern Yumen Basin (HSG-K and CG-K) are statistically different from those of Lower Cretaceous samples from the Qilian Shan (NQL-K and JTS-K) and southern Yumen Basin (HLX-K). Two groups of similarly sourced samples were then identified using the abovementioned metrics: (1) Samples HSG-K and CG-K, which are dominated by a single late Paleozoic-early Mesozoic population, (2) Samples NQL-K, JTS-K and HLX-K, which contain a cosmopolitan assemblage of all major detrital zircon populations.

Zircons from samples CG-K and HSG-K are dominated by age peaks at 290-230 Ma, which accounts for approximately 80% of the total dated grains (Fig. 8i-8j). The predominant late Paleozoic and early Mesozoic population and the absence of early Paleozoic and Precambrian ages suggest that the Bei Shan served as the source region for the clastic material deposited in the northern Yumen Basin (represented by the Caogou and Huoshaogou sections). This interpretation is consistent with the SSE-directed paleoflow reported from the Caogou and Huoshaogou section (Dai et al., 2005; Wang et al., 2016c). The detrital zircon ages distribution of sample HLX-K is complex, dispersed between ca. 3201 Ma and ca. 231 Ma, with a major age

peak of ca. 420 Ma (Fig. 8o). The early Paleozoic and Precambrian zircons account for ca. 90% of the total analyzed grains, indicative of a predominant Qilian Shan source during the early Cretaceous. However, in the Hongliuxia section, clast-supported conglomerate shows pebble-imbrication mainly trending towards the south and northwest (Peng, 2013). These multiple paleocurrent directions suggest that both the northern Qilian Shan and the Bei Shan shed materials into the Yumen Basin during that period. The zircon ages spectrum of sample NQL-K is characterized by a single peak at ca. 439 Ma and two potential sub-peaks at 1921-1600 Ma and ca. 270 Ma, respectively. This sample was collected from a thin sandstone lens within a thickly bedded massive conglomerate. The angular cobbles and boulders in the conglomerate are poorly sorted suggesting deposition from a proximal source (Fig. 5h-5i). Finally, the detrital zircon ages distribution in sample JTS-K is characterized by a Permian age peak, a Silurian age peak, and two age populations of 2.8-2.1 Ga and 2.1-1.0 Ga, similar to the age distribution of the modern samples collected from two parallel rivers draining the Qilian Shan (samples QL1 and QL2, Figs. 2, 3 and 8). Moreover, this Cretaceous sandstone sample was collected from a thin sandstone lens that developed in a massive conglomerate bed in the northern Qilian Shan (Figs. 2 and 3). The sandstone is poorly sorted with angular grains, suggesting that the particles have not been transported very far (Figs. 5i and 6e). This implies that the northern Qilian Shan served as a source for the sediments in the northern flank of northern Qilian Shan during the early Cretaceous.

Our detrital zircon geochronology study, together with previous paleocurrent analysis in this region, suggest that both the Bei Shan and the northern Qilian Shan served as two significant sources, shedding sediments into the Yumen Basin during the early Cretaceous. This is consistent with the thermochronometry data that suggest rapid initial basement cooling in both

regions during Cretaceous time (George et al., 2001; Gillespie et al., 2017; Jolivet et al., 2001; Li et al., 2013; Pan et al., 2013; Sobel et al., 2001). However, detrital zircons with early Paleozoic and Precambrian ages, which are distinctive indicators of the northern Qilian Shan source, were only found in Lower Cretaceous samples collected in the northern Qilian Shan (sample JTS-K) and the northern flank of the Qilian Shan (samples NQL-K and HLX-K). On the other hand, the U-Pb zircon age spectra of Lower Cretaceous samples (samples CG-K and HSG-K) from the Yumen Basin (Caogou and Huoshaogou sections) show a unimodal late Paleozoic age population, suggesting a unique source situated in the Bei Shan region. The south-directed drainage systems derived from the Bei Shan shed detritus in the Yumen Basin, whereas the materials eroded from the northern Qilian Shan appear to have been transported across the northern Qilian Shan, but deposited no further than the southern margin of the Yumen Basin.

The abovementioned provenance interpretation is consistent with our sandstone petrology analysis (Fig. 6f and 6g). Our sandstone petrographic results show that the Lower Cretaceous strata in the northern Qilian Shan (sample NQL-K) were sourced from a recycled orogen provenance setting. In contrast, the Lower Cretaceous strata in the Yumen Basin (samples CG-K, HSG-K and HLX-K) contain more feldspathic and quartzose compositions, showing a shift towards a continental block source (Fig. 6f and 6g). It is likely that the Qilian Shan (recycled orogen provenance) served as the predominant source for the sediments the northern Qilian Shan and southern Yumen Basin while the clastic materials in the northern Yumen Basin are mainly derived from Bei Shan (continental block provenance). According to the QFL ternary diagrams, the feldspar- and quartz-rich sandstones from the Yumen Basin may indicate a deep basement exposure of their source region (i.e. Bei Shan) during the early Cretaceous (Dickinson et al., 1983), rather than a shallow basement exposure that relates to a

thin-skinned fold-thrust system. Geologic survey also shows that the Paleozoic metasedimentary rocks, which are well-exposed within the Qilian Shan and on the north side of Bei Shan, are not exposed on the south side of Bei Shan, suggestive of a deeper basement exposure in the southern Bei Shan (Fig. 2; See Fig. 2 in He et al. (2018))(He et al., 2018; Li et al., 2012; Xiao et al., 2010). The evidence from deep basement exposure of southern Bei Shan as well as the evidence of the extensional features within the Yumen Basin during the early Cretaceous (Chen et al., 2014a; Peng, 2013; Yang et al., 2001; Yang et al., 2011) are consistent with recent observations of extensional tectonics. However, further effort should be made to unravel the early Cretaceous tectonic setting in the Bei Shan and Qilian Shan regions.

Although some studies have identified the facies and depositional environments of the Lower Cretaceous strata in the Yumen Basin (Peng, 2013; Yang et al., 2011), few studies have investigated the Lower Cretaceous strata within the Qilian Shan yet. In this study, the Lower Cretaceous proximal deposits in the northern Qilian Shan (Figs. 5h-5i, 6e) and the significant Qilian Shan source detrital zircon signature for the Lower Cretaceous strata samples (see samples NQL-K and JTS-K in Fig. 7t) from the northern Qilian Shan call for pre-existing topographic relief in the northeast margin of the Tibetan plateau prior to the India-Asia collision.

5.2 Quantitatively determined mixing proportions between the Qilian Shan and Bei Shan sources: implication for multiple stages of growth of the NE Tibetan plateau

The detrital zircon ages distribution of the two Cretaceous samples (samples CG-K and HSG-K), characterized by a unimodal late Paleozoic to Mesozoic age peak, are very similar to that of the late Oligocene – early Miocene samples (samples FZ1 and FZ2, see (Wang et al., 2016c)) collected in the Caogou section (Wang et al., 2016c) (Fig. 4). Previous provenance analysis determined that those late Oligocene - early Miocene strata were mainly derived from

Bei Shan region (Wang et al., 2016b). In the northeastern edge of the Tibetan plateau, the base of the middle Eocene to Oligocene strata unconformably overlies the Cretaceous strata (Dai et al., 2005; Wang et al., 2016b) (Figs. 4, 5b, 5d and 5f), and the absence of Paleocene and early Eocene strata in this region make it difficult to constrain the paleotopography during the early Paleogene. Nonetheless, the similar detrital zircon ages distribution between the Lower Cretaceous and Oligocene samples as well as the consistent paleocurrent patterns over that period of time indicate that the source of the material deposited in the Yumen Basin (Caogou and Huoshaogou sections) was stable. Bovet et al. (2009) argued that the paucity of Paleocene and Eocene deposits in the northern Qilian Shan and in the Yumen Basin may reflect that structures in both northern Qilian Shan and Yumen Basin became inactive, and non-sedimentation (or weak erosion) dominated in these areas, possibly a result of sustained high topography. Alternatively, compressive deformation within the both northern Qilian Shan and Yumen Basin would potentially lead to continuous erosion that formed the unconformity between Cretaceous and Eocene strata. This uncertainty highlights the need for further effort on determining the growth history of the NE Tibetan plateau from the late Cretaceous to early Eocene.

While simply comparing the detrital zircon age spectra of each sample could reveal general source variation, quantitative analysis helps to elucidate the exact contribution of Qilian Shan and Bei Shan sources through time. This information, combined with the existing sedimentology and low-temperature thermochronology datasets, contributes to a better understating of the distribution of relief in the Qilian Shan and the NE Tibetan plateau. To quantitatively determine mixing proportions between the Qilian Shan and Bei Shan sources, we use the newly developed MATLAB-based DZmix Inverse Monte Carlo method (Sundell and Saylor, 2017). This program yields a single best-fit (highest cross-correlation coefficient R^2) inverse Monte Carlo model result

for each tested sample (see the pink solid lines in Figure 9) and estimates the respective contributions of the known Qilian Shan and Bei Shan sources for each sample. The Qilian Shan source input is represented by two modern river sand samples QL1 and QL2, and the Bei Shan source input is represented by two modern river sand samples BS2 and BS3. Inverse Monte Carlo model results for each tested sample are presented in Figure 9. Results shows that in the northern Yumen Basin, 100% of the material was derived from basement rocks of the Bei Shan during the Cretaceous (sample HSG-K and CG-K; Fig. 9b, 9d). During the late Oligocene (23.8 Ma, sample FZ1, Fig. 9f), 98% of materials in the northern Yumen Basin are derived from basement rocks of the Bei Shan with only 2% of Qilian Shan sourced debris. However, the contribution of the Qilian Shan source to the northern Yumen Basin increased to 30-48% during the early Miocene (20.6-16.3 Ma, samples FZ2 and FZ3, Fig. 9h and 9j) and dramatically increased to 87-91% during the middle Miocene (15.8-13.1 Ma, samples FZ4 and FZ5, Fig. 9l and 9n). During the late Miocene (7.8 Ma, sample FZ7, Fig. 9p), 82% of the clastic material is derived from basement rocks of the Qilian Shan with 18% from the Bei Shan source. The best-fit inverse Monte Carlo model results further reinforce the conclusion that the Bei Shan was the predominant source of the clastic material deposited in the northern Yumen Basin from the early Cretaceous to the late Oligocene. The contribution of the Qilian Shan basement rocks to the sediments in the Yumen Basin significantly increased during the Miocene, especially during the middle Miocene, which we interpret as the growth of the Qilian Shan. (Fig. 9). Moreover, by simply comparing the detrital zircon spectra of each Cenozoic sample, Wang et al. (2016c) have revealed that a change in source area occurred at ~16.7 Ma in the Yumen Basin. Our quantitative analysis shows the contribution of the Qilian Shan source to the northern Yumen Basin significantly increased from 2% to 30% at ~20.8 Ma. We interpret this early Miocene initial

source change as the onset of growth of the Qilian Shan.

In addition, various lines of investigation, including evidence from (1) thermochronology studies on the Cenozoic strata in the Yumen Basin (He et al., 2017; Wang et al., 2016b; Zheng et al., 2017a) and on the basement rocks in the northern Qilian Shan (Pan et al., 2013; Zheng et al., 2010), (2) magnetostratigraphic studies of sediment accumulation rates in the Yumen Basin (Wang et al., 2016b), (3) stratigraphy and provenance analysis (Bovet et al., 2009; Lease et al., 2012; Wang et al., 2016c), and (4) sediment color and grain-size studies from sediments preserved in the Yumen Basin (Wang et al., 2016d), have suggested a middle Miocene rapid growth of northern Qilian Shan. We thus infer that the palaeogeography in this region largely stable from the late Cretaceous to late Oligocene time and was then modified since the early Miocene in response to the reactivation of the Qilian Shan region (Bovet et al., 2009; Wang et al., 2016b; Wang et al., 2016c; Wang et al., 2016d; Yue et al., 2004a; Zheng et al., 2010) (Fig. 10). Given the growing evidence for Oligocene-early Miocene reactivation of deformation in Xianshuihe fault system, Kunlun Shan, Tian Shan, and even the Sayan ranges and Baikal rift system in Siberia to the north (Clark et al., 2010; Hendrix, 2000; Jolivet et al., 2013a; Jolivet et al., 2009; Xu and Kamp, 2000), it is likely that stress has been transferred to the margins of the Tibetan plateau, and even beyond the plateau to the north since India -Asian collision. Considering the pre-existing Cretaceous positive topography of the Qilian Shan with the Miocene rapid growth of the central-northern Qilian Shan and late Miocene growth of the northern Qilian Shan, we suggest multiple stages of range growth in the Qilian Shan during the Mesozoic and Cenozoic (Fig. 10), similar to that already documented in other parts of northern Tibet (Cheng et al., 2016a; He et al., 2017; Lease et al., 2012; Wang et al., 2013; Wang et al., 2017d; Yuan et al., 2013).

Figure 9. Unmixing detrital geochronology age distribution. (a), (c), (e), (g), (I), (k), (m) and (o) Cumulative distribution plot (CDF) of each sample, together with CDFs of modern river sample from Bei Shan (BS2 and BS3) and Qilian Shan (QL1 and QL2). Light green and dark green solid lines refer to sample BS2 and BS3, respectively. Light blue and dark blue solid lines refer to the sample BS2 and BS3, respectively. The black solid line refers to each tested sample (FZ1-FZ5, FZ7, CG-K and HSG-K). (b), (d), (f), (h), (j), (l), (n) and (p) Inverse Monte Carlo results using cross-correlation coefficient R^2 as probability density plot (PDP). The black line refers to the PDP of each tested sample (FZ1-FZ5, FZ7, CG-K and HSG-K). The pink solid line refers to PDP of the best optimized model result of each sample after running the Inverse Monte Carlo program. The Inverse Monte Carlo software package, DZmix (Sundell and Saylor, 2017), is used to quantify source mixing proportions. The pie charts show the contribution of the Bei Shan source and Qilian Shan source. Note that the Qilian Shan source dramatically increases from 2% to 48% during the Miocene, which we interpret as the growth of the Qilian Shan. The age of the strata is based on previous sedimentary and magnetostratigraphy studies (Peng, 2013; Wang et al., 2016b).

5.3 Implication for the eastern termination of the Altyn Tagh Fault

Provenance results also imply that the Cenozoic ATF likely died out within the Yumen Basin and have not extended further eastward since its Eocene or Miocene initiation. For instance, previous studies have revealed an >300 km post-Cretaceous offset along the ATF (Cheng et al., 2015a; Cheng et al., 2016b; Ritts and Biffi, 2000; Yin and Harrison, 2000; Yin et al., 2002). If the ATF extended beyond the Yumen Basin and linked with the strike-slip faults of

the Alxa or regions further to the east (Darby et al., 2005; Yue and Liou, 1999), hundreds of kilometers of sinistral strike-slip motion along the ATF during the Cenozoic would not have been transferred to the oblique thrusting in the Qilian Shan. In other words, the Yumen Basin would have been approximately located near the present-day position of the Suganhu Basin during the Cretaceous after restoring the >300 km sinistral post-Cretaceous offset along the ATF (Fig. 2a). In this case, the Yumen Basin would have received materials eroded from the Dunhuang terrane to the northwest (Fig. 2a). Apatite and zircon fission track data suggest that the Dunhuang terrane has been exhumed no later than the late Triassic-early Jurassic (Jolivet et al., 2001). Given that the basement of the Dunhuang terrane is characterized by a predominant proportion of Archean and Proterozoic rocks (He et al., 2018; Long et al., 2014; Zhao et al., 2015), the detrital zircon ages spectra of the Cretaceous samples from the Yumen Basin should contain a significant amount of Archean and Proterozoic zircon ages. In addition, the proportions of those Precambrian ages populations would vary from Cretaceous to late Oligocene time due to the left-lateral displacement along the ATF (Cheng et al., 2016b; Yue et al., 2004b). The absence of Precambrian zircons in the Cretaceous samples (samples CG-K and HLX-K, Figs. 8 and 9), as well as the consistently similar detrital zircon ages spectra of the samples from the lower Cretaceous to the early Miocene strata in the Yumen Basin require that the ATF terminated in the western Yumen Basin and has not been linked to strike-slip faults in the Alxa or regions further to the east since its Eocene or Miocene initiation. This conclusion is in agreement with independent, albeit indirect evidence suggesting that the ATF died out within the Yumen Basin since its initiation, including: (1) the limited (<50 km) offset of the Jurassic and Cretaceous strata in the western Yumen Basin (Fig. 2); (2) the high resistivity crust of the Huahai-Jinta Basin (Xiao et al., 2015) which prevents the ATF from passing through (Fig. 10a); and (3) the dramatic

eastward decrease in the left-lateral slip rate along the eastern end of the ATF (Burchfiel et al., 1989; Mériaux et al., 2005; Meyer et al., 1998; Xu et al., 2005; Zhang et al., 2007b; Zheng et al., 2013b) (Fig. 10a).

Figure 10. (a) Geological map showing slip rates on faults in the Yumen Basin and northern Qilian Shan, modified from (Zheng et al., 2013a). The slip rate on each fault is from previous work (Chen, 2003; Hetzel et al., 2002; Min et al., 2002; Xu et al., 2005; Zheng, 2009; Zheng et al., 2013a; Zheng et al., 2013b). Note that the horizontal slip rate on faults generally decrease eastwards. H: Horizontal slip rate; V: Vertical slip rate; S: Shortening rate across fault. (b) Schematic models illustrating the topographic variation of the Yumen Basin and northern Qilian Shan, during the Miocene and Cretaceous.

6. Conclusion

Our provenance analysis reveals that both the northern Qilian Shan and the Bei Shan served as the two most straightforward source regions for the clastic material deposited in the Yumen Basin during the early Cretaceous. South-directed drainage systems derived from the Bei Shan largely shed detritus into the Yumen Basin, whereas the materials eroded from the northern Qilian Shan were transported across the northern Qilian Shan reaching as far as the southern margin of the Yumen Basin. Combined with existing sedimentology and low-temperature thermochronology datasets, our field investigation and sandstone petrography analysis as well as detrital zircon geochronology results, indicate Cretaceous topography in the northeast margin of the Tibetan plateau prior to the India-Asia collision.

After extracting mixing proportions of source regions, our quantitative estimates show that 98-80% of materials in the northern Yumen Basin are derived from basement rocks of the Bei Shan from Cretaceous to late Oligocene time, whereas the contribution of the Qilian Shan source to the northern Yumen Basin increased to 30-48% during the early Miocene. The consistently similar detrital zircon ages distribution in the Cretaceous to late Oligocene samples suggests that the palaeogeography in the northeastern edge of the plateau has been largely stable from Cretaceous to late Oligocene times, and was modified during the early Miocene in response to the uplift of the northern Qilian Shan. Our results highlight the multiple-phase tectonic history of the northeastern Tibetan plateau. We further conclude that the Altyn Tagh Fault terminated within the western Yumen Basin and has not been linked to strike-slip faults in the Alxa or regions further to the east since its initiation.

Acknowledgments

The research was funded by grants from the National Science Foundation (EAR-1348005 and OISE-1545859) to Garzione, Open project fund from State Key Laboratory of Loess and Quaternary Geology, Institute of Earth Environment, CAS (No. SKLLQG1701) to Cheng, and National Science and Technology Major Project of China (Grant 2017ZX05008-001) to Guo. We are grateful to Editor-in-Chief Dr. M. Santosh, Associate Editor Dr. Zeming Zhang, Dr. Kendra Murray and an anonymous reviewer for constructive comments that improved the paper. We gratefully acknowledge Mark Pecha, Nicky Giesler, Heather Alvarez, Mekha Pereira and Arizona Laserchron Center for their help with detrital zircon analysis. SRTM digital topography is from http://www2.jpl.nasa.gov/srtm.

References

Allen, M.B., Walters, R.J., Song, S., Saville, C., De Paola, N., Ford, J., Hu, Z., Sun, W., 2017. Partitioning of oblique convergence coupled to the fault locking behavior of fold‐and‐thrust belts: Evidence from the Qilian Shan, northeastern Tibetan Plateau. Tectonics 36, 1679-1698.

Belousova, E., Griffin, W.L., O'reilly, S.Y., Fisher, N., 2002. Igneous zircon: trace element composition as an indicator of source rock type. Contrib Mineral Petrol 143, 602-622.

Bovet, P.M., Ritts, B.D., Gehrels, G., Abbink, A.O., Darby, B., Hourigan, J., 2009. Evidence of Miocene crustal shortening in the north Qilian Shan from Cenozoic stratigraphy of the western Hexi Corridor, Gansu Province, China. American Journal of Science 309, 290-329.

Burchfiel, B.C., Quidong, D., Molnar, P., Royden, L., Yipeng, W., Peizhen, Z., Weiqi, Z., 1989. Intracrustal detachment within zones of continental deformation. Geology 17, 748-752.

Chen, S., Wang, H., Wei, J., Lv, Z., Gan, H., Jin, S., 2014a. Sedimentation of the Lower Cretaceous Xiagou Formation and its response to regional tectonics in the Qingxi Sag, Jiuquan Basin, NW China. Cretaceous Research 47, 72-86.

Chen, W., 2003. Principal tectonic deformation features and their generation mechanism in the Hexi Corridor and its adjacent regions since the late Quaternary. Institute of Geology, China Earthquake Administration, Beijing, Beijing, p. 87.

Chen, Y., Gilder, S., Halim, N., Cogné, J.P., Courtillot, V., 2002. New paleomagnetic constraints on central Asian kinematics: Displacement along the Altyn Tagh fault and rotation of the Qaidam Basin. Tectonics 21, 1042.

Chen, Y., Song, S., Niu, Y., Wei, C., 2014b. Melting of continental crust during subduction initiation: A case study from the Chaidanuo peraluminous granite in the North Qilian suture zone. Geochimica et Cosmochimica Acta 132, 311-336.

Chen, Y., Xia, X., Song, S., 2012. Petrogenesis of Aoyougou high-silica adakite in the North Qilian orogen, NW China: Evidence for decompression melting of oceanic slab. Chinese science bulletin, 1-13.

Cheng, F., Fu, S., Jolivet, M., Zhang, C., Guo, Z., 2016a. Source to sink relation between the Eastern Kunlun Range and the Qaidam Basin, northern Tibetan Plateau, during the Cenozoic. Geological Society of America Bulletin 128, 258-283.

Cheng, F., Guo, Z., Jenkins, H.S., Fu, S., Cheng, X., 2015a. Initial rupture and displacement on the Altyn Tagh fault, northern Tibetan Plateau: Constraints based on residual Mesozoic to Cenozoic strata in the western Qaidam Basin. Geosphere 11, 921-942.

Cheng, F., Jolivet, M., Dupont-Nivet, G., Wang, L., Yu, X., Guo, Z., 2015b. Lateral extrusion along the Altyn Tagh Fault, Qilian Shan (NE Tibet): insight from a 3D crustal budget. Terra Nova 27, 416-425.

Cheng, F., Jolivet, M., Fu, S., Zhang, C., Zhang, Q., Guo, Z., 2016b. Large-scale displacement along the Altyn Tagh Fault (North Tibet) since its Eocene initiation: Insight from detrital zircon U–Pb geochronology and subsurface data. Tectonophysics 677–678, 261-279.

Cheng, F., Jolivet, M., Hallot, E., Zhang, D., Zhang, C., Guo, Z., 2017. Tectono-magmatic rejuvenation of the Qaidam craton, northern Tibet. Gondwana Research 49, 248-263.

Clark, M.K., Farley, K.A., Zheng, D., Wang, Z., Duvall, A.R., 2010. Early Cenozoic faulting of the northern Tibetan Plateau margin from apatite (U–Th)/He ages. Earth and Planetary Science Letters 296, 78-88.

Cowgill, E., Yin, A., Harrison, T.M., Xiao-Feng, W., 2003. Reconstruction of the Altyn Tagh fault based on U-Pb geochronology: Role of back thrusts, mantle sutures, and heterogeneous crustal strength in forming the Tibetan Plateau. Journal of Geophysical Research 108, 2346.

Dai, S., Fang, X., Song, C., Gao, J., Gao, D., Li, J., 2005. Early tectonic uplift of the northern Tibetan Plateau. CHINESE SCIENCE BULLETIN-ENGLISH EDITION- 50, 1642.

Darby, B.J., Ritts, B.D., Yue, Y., Meng, Q., 2005. Did the Altyn Tagh fault extend beyond the Tibetan Plateau? Earth and Planetary Science Letters 240, 425-435.

Decelles, P.G., Robinson, D.M., Zandt, G., 2002. DeCelles, P. G., Robinson, D. M. & Zandt, G. Implications of shortening in the Himalayan fold-thrust belt for uplift of the Tibetan plateau. Tectonics 21, 1062. Tectonics 21, 12-11-12-25.

Dewey, J.F., Shackleton, R.M., Chengfa, C., Yiyin, S., 1988. The Tectonic Evolution of the Tibetan Plateau. Philosophical Transactions of the Royal Society of London. Series A, Mathematical and Physical Sciences 327, 379-413.

Dickinson, W.R., Beard, L.S., Brakenridge, G.R., Erjavec, J.L., Ferguson, R.C., Inman, K.F., Knepp, R.A., Lindberg, F.A., Ryberg, P.T., 1983. Provenance of North American Phanerozoic sandstones in relation to tectonic setting. Geological Society of America Bulletin 94, 222-235.

Dickinson, W.R., Suczek, C.A., 1979. Plate tectonics and sandstone compositions. Aapg Bulletin 63, 2164-2182.

Ding, L., Xu, Q., Yue, Y., Wang, H., Cai, F., Li, S., 2014. The Andean-type Gangdese Mountains: Paleoelevation record from the Paleocene–Eocene Linzhou Basin. Earth and Planetary Science Letters 392, 250-264.

Duan, J., Li, C., Qian, Z., Jiao, J., 2015. Geochronological and geochemical constraints on the petrogenesis and tectonic significance of Paleozoic dolerite dykes in the southern margin of Alxa Block, North China Craton. Journal of Asian Earth Sciences 111, 244-253.

Dupont-Nivet, G., Horton, B., Butler, R., Wang, J., Zhou, J., Waanders, G., 2004. Paleogene clockwise tectonic rotation of the Xining-Lanzhou region, northeastern Tibetan Plateau. J. Geophys. Res 109, B04401.

England, P., Searle, M., 1986. The Cretaceous‐Tertiary deformation of the Lhasa block and its implications for crustal thickening in Tibet. Tectonics 5, 1-14.

Enkelmann, E., Ratschbacher, L., Jonckheere, R., Nestler, R., Fleischer, M., Gloaguen, R., Hacker, B.R., Zhang, Y.Q., Ma, Y.-S., 2006. Cenozoic exhumation and deformation of northeastern Tibet and the Qinling: Is Tibetan lower crustal flow diverging around the Sichuan Basin? Geological Society of America Bulletin 118, 651-671.

Fedo, C.M., Sircombe, K.N., Rainbird, R.H., 2003. Detrital zircon analysis of the sedimentary record. Reviews in mineralogy and geochemistry 53, 277-303.

Gehrels, G., 2014. Detrital Zircon U-Pb Geochronology Applied to Tectonics. Annual Review of Earth and Planetary Sciences 42, 127-149.

Gehrels, G., Pecha, M., 2014. Detrital zircon U-Pb geochronology and Hf isotope geochemistry of Paleozoic and Triassic passive margin strata of western North America. Geosphere 10, 49-65.

Gehrels, G., Valencia, V., Pullen, A., 2006. Detrital zircon geochronology by laser-ablation multicollector ICPMS at the Arizona LaserChron Center. The Paleontological Society Papers 12, 67-76.

Gehrels, G.E., Valencia, V.A., Ruiz, J., 2008. Enhanced precision, accuracy, efficiency, and spatial resolution of U‐Pb ages by laser ablation−multicollector−inductively coupled plasma−mass spectrometry. Geochemistry, Geophysics, Geosystems 9.

Gehrels, G.E., Yin, A., Wang, X.F., 2003a. Detrital-zircon geochronology of the northeastern Tibetan plateau. Geological Society of America Bulletin 115, 881-896.

Gehrels, G.E., Yin, A., Wang, X.F., 2003b. Magmatic history of the northeastern Tibetan Plateau. Journal of Geophysical Research 108, 2423.

George, A.D., Marshallsea, S.J., Wyrwoll, K.-H., Jie, C., Yanchou, L., 2001. Miocene cooling in the northern Qilian Shan, northeastern margin of the Tibetan Plateau, revealed by apatite fission-track and vitrinite-reflectance analysis. Geology 29, 939-942.

Gillespie, J., Glorie, S., Xiao, W., Zhang, Z., Collins, A.S., Evans, N., McInnes, B., De Grave, J., 2017. Mesozoic reactivation of the Beishan, southern Central Asian Orogenic Belt: Insights from low-temperature thermochronology. Gondwana Research 43, 107-122.

Gong, H., Zhao, H., Xie, W., Kang, W., Zhang, R., Yang, L., Zhang, Y., Song, J., Zhang, Y., 2017. Tectono-thermal events of the North Qilian Orogenic Belt, NW China: Constraints from detrital zircon U-Pb ages of Heihe River sediments. Journal of Asian Earth Sciences 138, 647-656.

He, P., Song, C., Wang, Y., Chen, L., Chang, P., Wang, Q., Ren, B., 2017. Cenozoic exhumation in the Qilian Shan, northeastern Tibetan Plateau: Evidence from detrital fission track thermochronology in the Jiuquan Basin. Journal of Geophysical Research: Solid Earth 122, 6910-6927.

He, Z.-Y., Klemd, R., Yan, L.-L., Zhang, Z.-M., 2018. The origin and crustal evolution of microcontinents in the Beishan orogen of the southern Central Asian Orogenic Belt. Earth-Science Reviews.

Hendrix, M.S., 2000. Evolution of Mesozoic Sandstone Compositions, Southern Junggar, Northern Tarim, and Western Turpan Basins, Northwest China: A Detrital Record of the Ancestral Tian Shan. Journal of Sedimentary Research 70, 520-532.

Hetzel, R., Niedermann, S., Tao, M., Kubik, P.W., Ivy-Ochs, S., Gao, B., Strecker, M.R., 2002. Low slip rates and long-term preservation of geomorphic features in Central Asia. Nature 417, 428-432.

Hilgen, F., Lourens, L., van Dam, J.A., 2012. The neogene period.

Hoskin, P., Black, L., 2000. Metamorphic zircon formation by solid‐state recrystallization of protolith igneous zircon. Journal of metamorphic Geology 18, 423-439.

Ingersoll, R.V., Bullard, T.F., Ford, R.L., Grimm, J.P., Pickle, J.D., Sares, S.W., 1984. The effect of grain size on detrital modes: a test of the Gazzi-Dickinson point-counting method. Journal of Sedimentary Research 54, 103-116.

Jolivet, M., Arzhannikov, S., Arzhannikova, A., Chauvet, A., Vassallo, R., Braucher, R., 2013a. Geomorphic Mesozoic and Cenozoic evolution in the Oka-Jombolok region (East Sayan ranges, Siberia). Journal of Asian Earth Sciences 62, 117-133.

Jolivet, M., Arzhannikov, S., Arzhannikova, A., Chauvet, A., Vassallo, R., Braucher, R., 2013b. Geomorphic Mesozoic and Cenozoic evolution in the Oka-Jombolok region (East Sayan ranges, Siberia). Journal of Asian Earth Sciences 62, 117-133.

Jolivet, M., Brunel, M., Seward, D., Xu, Z., Yang, J., Roger, F., Tapponnier, P., Malavieille, J., Arnaud, N., Wu, C., 2001. Mesozoic and Cenozoic tectonics of the northern edge of the Tibetan plateau: fission-track constraints. Tectonophysics 343, 111-134.

Jolivet, M., De Boisgrollier, T., Petit, C., Fournier, M., Sankov, V.A., Ringenbach, J.C., Byzov, L., Miroshnichenko, A.I., Kovalenko, S.N., Anisimova, S.V., 2009. How old is the Baikal Rift Zone? Insight from apatite fission track thermochronology. Tectonics 28, TC3008.

Jolivet, M., Dominguez, S., Charreau, J., Chen, Y., Li, Y., Wang, Q., 2010. Mesozoic and Cenozoic tectonic history of the central Chinese Tian Shan: Reactivated tectonic structures and active deformation. Tectonics 29.

Kapp, P., DeCelles, P., Leier, A., Fabijanic, J., He, S., Pullen, A., Gehrels, G., Ding, L., 2007a. The Gangdese retroarc thrust belt revealed. GSA Today 17, 4.

Kapp, P., DeCelles, P.G., Gehrels, G.E., Heizler, M., Ding, L., 2007b. Geological records of the Lhasa-Qiangtang and Indo-Asian collisions in the Nima area of central Tibet. Geological Society of America Bulletin 119, 917-933.

Kapp, P., Yin, A., Harrison, T.M., Ding, L., 2005. Cretaceous-Tertiary shortening, basin development, and volcanism in central Tibet. Geological Society of America Bulletin 117, 865-878.

Lease, R.O., 2014. Cenozoic mountain building on the northeastern Tibetan Plateau. Geological Society of America Special Papers 507, 115-127.

Lease, R.O., Burbank, D.W., Hough, B., Wang, Z., Yuan, D., 2012. Pulsed Miocene range growth in northeastern Tibet: Insights from Xunhua Basin magnetostratigraphy and provenance. Geological Society of America Bulletin 124, 657-677.

Leier, A.L., Kapp, P., Gehrels, G.E., DeCelles, P.G., 2007. Detrital zircon geochronology of Carboniferous–Cretaceous strata in the Lhasa terrane, Southern Tibet. Basin Research 19, 361-378.

Li, L., Garzione, C.N., Pullen, A., Zhang, P., Li, Y., 2017. Late Cretaceous− Cenozoic basin evolution and topographic growth of the Hoh Xil Basin, central Tibetan Plateau. GSA Bulletin.

Li, Q., Pan, B., Hu, X., Hu, Z., Li, F., Yang, S., 2013. Apatite fission track constraints on the pattern of faulting in the north Qilian Mountain. Journal of Earth Science 24, 569-578.

Li, S., Wang, T., Wilde, S.A., Tong, Y., Hong, D., Guo, Q., 2012. Geochronology, petrogenesis and tectonic implications of Triassic granitoids from Beishan, NW China. Lithos 134, 123-145.

Li, Z., Song, W., Peng, S., Wang, D., Zhang, Z., 2004. Mesozoic–Cenozoic tectonic relationships between the Kuqa subbasin and Tian Shan, northwest China: constraints from depositional records. Sedimentary Geology 172, 223-249.

Licht, A., Pullen, A., Kapp, P., Abell, J., Giesler, N., 2016. Eolian cannibalism: Reworked loess and fluvial sediment as the main sources of the Chinese Loess Plateau. GSA Bulletin 128, 944-956.

Lippert, P.C., Hinsbergen, D.J.J.V., Dupont-Nivet, G., 2014. The Early Cretaceous to present latitude of the central Lhasa-plano (Tibet): A paleomagnetic synthesis with implications for Cenozoic tectonics, paleogeography, and climate of Asia. Special Paper of the Geological Society of America 507, 1-21.

Liu, J., Zhang, P., Lease, R.O., Zheng, D., Wan, J., Wang, W., Zhang, H., 2013. Eocene onset and late Miocene acceleration of Cenozoic intracontinental extension in the North Qinling range–Weihe graben: Insights from apatite fission track thermochronology. Tectonophysics 584, 281-296.

Long, X., Yuan, C., Sun, M., Kröner, A., Zhao, G., 2014. New geochemical and combined zircon U–Pb and Lu–Hf isotopic data of orthogneisses in the northern Altyn Tagh, northern margin of the Tibetan plateau: Implication for Archean evolution of the Dunhuang Block and crust formation in NW China. Lithos 200–201, 418-431.

Lu, S.N., Li, H.K., Zhang, C.L., Niu, G.H., 2008. Geological and geochronological evidence for the Precambrian evolution of the Tarim Craton and surrounding continental fragments. Precambrian Research 160, 94-107.

Ludwig, K., 2008. A geochronological toolkit for Microsoft Excel: Berkeley Geochronology Center Special Publication v. 4.

Mériaux, A.S., Tapponnier, P., Ryerson, F., Xiwei, X., King, G., Van der Woerd, J., Finkel, R., Haibing, L., Caffee, M., Zhiqin, X., 2005. The Aksay segment of the northern Altyn Tagh fault: Tectonic geomorphology, landscape evolution, and Holocene slip rate. Journal of Geophysical Research: Solid Earth 110.

Métivier, F., Gaudemer, Y., Tapponnier, P., Meyer, B., 1998. Northeastward growth of the Tibet plateau deduced from balanced reconstruction of two depositional areas: The Qaidam and Hexi Corridor basins, China. Tectonics 17, 823-842.

Meyer, B., Tapponnier, P., Bourjot, L., Metivier, F., Gaudemer, Y., Peltzer, G., Shunmin, G., Zhitai, C., 1998. Crustal thickening in Gansu‐Qinghai, lithospheric mantle subduction, and oblique, strike‐slip controlled growth of the Tibet plateau. Geophysical Journal International 135, 1-47.

Min, W., Zhang, P., Li, C., Mao, F., Zhang, S., 2002. Research on the active faults and paleoearthquakes in the western Jiuquan basin. Seismology and Geology 24, 35-44.

Molnar, P., Tapponnier, P., 1975. Cenozoic tectonics of Asia: Effects of a continental collision. Science 189, 419-426.

Murphy, M., Yin, A., Harrison, T., Dürr, S., Chen, Z., Ryerson, F., Kidd, W., Wang, X., Zhou, X., 1997. Did the Indo-Asian collision alone create the Tibetan plateau? Geology 25, 719-722.

Pan, B., Li, Q., Hu, X., Geng, H., Liu, Z., Jiang, S., Yuan, W., 2013. Cretaceous and Cenozoic cooling history of the eastern Qilian Shan, north-eastern margin of the Tibetan Plateau: evidence from apatite fission-track analysis. Terra Nova 25, 431-438.

Peng, N., 2013. Basin Analysis and Paleogeography in North Qilian Mountain to Beishan Area, Early Cretaceous, China Univerisity of Geosciences, Beijing. China Univerisity of Geosciences, Beijing, pp. 1-155.

Pullen, A., Ibáñez-Mejía, M., Gehrels, G.E., Ibáñez-Mejía, J.C., Pecha, M., 2014. What happens when n= 1000? Creating large-n geochronological datasets with LA-ICP-MS for geologic investigations. Journal of Analytical Atomic Spectrometry 29, 971-980.

Pullen, A., Kapp, P., Gehrels, G.E., DeCelles, P.G., Brown, E.H., Fabijanic, J.M., Ding, L., 2008. Gangdese retroarc thrust belt and foreland basin deposits in the Damxung area, southern Tibet. Journal of Asian Earth Sciences 33, 323-336.

Ritts, B.D., Biffi, U., 2000. Magnitude of post-Middle Jurassic (Bajocian) displacement on the central Altyn Tagh fault system, northwest China. Geological Society of America Bulletin 112, 61-74.

Roger, F., Jolivet, M., Cattin, R., Malavieille, J., 2011. Mesozoic-Cenozoic tectonothermal evolution of the eastern part of the Tibetan Plateau (Songpan-Garzê, Longmen Shan area): insights from thermochronological data and simple thermal modelling. Geological Society, London, Special Publications 353, 9-25.

Searle, M., Elliott, J., Phillips, R., Chung, S.-L., 2011. Crustal–lithospheric structure and continental extrusion of Tibet. Journal of the Geological Society 168, 633-672.

Sobel, E.R., Arnaud, N., Jolivet, M., Ritts, B.D., Brunel, M., 2001. Jurassic to Cenozoic exhumation history of the Altyn Tagh range, northwest China, constrained by 40Ar/39Ar and apatite fission track thermochronology. Geological Society of America Memoirs 194, 247-267.

Song, S., Niu, Y., Su, L., Xia, X., 2013. Tectonics of the North Qilian orogen, NW China. Gondwana Research 23, 1378-1401.

Song, S., Niu, Y., Zhang, L., Wei, C., Liou, J.G., Su, L., 2009. Tectonic evolution of early Paleozoic HP metamorphic rocks in the North Qilian Mountains, NW China: new perspectives. Journal of Asian Earth Sciences 35, 334-353.

Stacey, J.t., Kramers, J., 1975. Approximation of terrestrial lead isotope evolution by a two-stage model. Earth and planetary science letters 26, 207-221.

Staisch, L.M., Niemi, N.A., Hong, C., Clark, M.K., Rowley, D.B., Currie, B., 2014. A Cretaceous‐Eocene depositional age for the Fenghuoshan Group, Hoh Xil Basin: Implications for the tectonic evolution of the northern Tibet Plateau. Tectonics 33, 281-301.

Stevens, T., Carter, A., Watson, T., Vermeesch, P., Andò, S., Bird, A., Lu, H., Garzanti, E., Cottam, M., Sevastjanova, I., 2013. Genetic linkage between the Yellow River, the Mu Us desert and the Chinese Loess Plateau. Quaternary Science Reviews 78, 355-368.

Sundell, K.E., Saylor, J.E., 2017. Unmixing detrital geochronology age distributions. Geochemistry, Geophysics, Geosystems 18, 2872-2886.

Tapponnier, P., Meyer, B., Avouac, J.P., Peltzer, G., Gaudemer, Y., Shunmin, G., Hongfa, X., Kelun, Y., Zhitai, C., Shuahua, C., 1990. Active thrusting and folding in the Qilian Shan, and decoupling between upper crust and mantle in northeastern Tibet. Earth and Planetary Science Letters 97, 382387-383403.

Tapponnier, P., Xu, Z.Q., Roger, F., Meyer, B., Arnaud, N., Wittlinger, G., Yang, J.S., 2001. Oblique stepwise rise and growth of the Tibet Plateau. Science 294, 1671-1677.

Thomas, W.A., 2011. Detrital-zircon geochronology and sedimentary provenance. Lithosphere 3, 304-308.

Tian, Y., Kohn, B.P., Phillips, D., Hu, S., Gleadow, A.J., Carter, A., 2016a. Late Cretaceous−earliest Paleogene deformation in the Longmen Shan fold‐and‐thrust belt, eastern Tibetan Plateau margin: Pre‐Cenozoic thickened crust? Tectonics 35, 2293-2312.

Tian, Z., Xiao, W., Zhang, Z., Lin, X., 2016b. Fisson-track constrains on superposed folding in the Beishan orogenic belt, southernmost Altaids. Geoscience Frontiers 7, 181-196.

Tseng, C.-Y., Yang, H.-J., Yang, H.-Y., Liu, D., Tsai, C.-L., Wu, H., Zuo, G., 2007. The Dongcaohe ophiolite from the North Qilian Mountains: a fossil oceanic crust of the Paleo-Qilian ocean. Chinese Science Bulletin 52, 2390-2401.

Tung, K., Yang, H.-J., Yang, H.-Y., Liu, D., Zhang, J., Wan, Y., Tseng, C.-Y., 2007. SHRIMP U-Pb geochronology of the zircons from the Precambrian basement of the Qilian Block and its geological significances. Chinese Science Bulletin 52, 2687-2701.

Tung, K.-a., Yang, H.-y., Yang, H.-j., Smith, A., Liu, D., Zhang, J., Wu, C., Shau, Y.-h., Wen, D.-j., Tseng, C.-y., 2016. Magma sources and petrogenesis of the early–middle Paleozoic backarc granitoids from the central part of the Qilian block, NW China. Gondwana Research 38, 197-219.

Vermeesch, P., 2013. Multi-sample comparison of detrital age distributions. Chemical Geology 341, 140-146.

Volkmer, J.E., Kapp, P., Guynn, J.H., Lai, Q., 2007. Cretaceous‐Tertiary structural evolution of the north central Lhasa terrane, Tibet. Tectonics 26.

Wang, C., Li, R.-S., Smithies, R.H., Li, M., Peng, Y., Chen, F.-N., He, S.-P., 2017a. Early Paleozoic felsic magmatic evolution of the western Central Qilian belt, Northwestern China, and constraints on convergent margin processes. Gondwana Research 41, 301-324.

Wang, E., Xu, F.-Y., Zhou, J.-X., Wan, J., Burchfiel, B.C., 2006. Eastward migration of the Qaidam basin and its implications for Cenozoic evolution of the Altyn Tagh fault and associated river systems. Geological Society of America Bulletin 118, 349-365.

Wang, J.G., Hu, X., Garzanti, E., Ji, W.Q., Liu, Z.C., Liu, X.C., Wu, F.Y., 2017b. Early cretaceous topographic growth of the Lhasaplano, Tibetan plateau: Constraints from the Damxung conglomerate. Journal of Geophysical Research: Solid Earth 122, 5748-5765.

Wang, T., Wang, Z., Yan, Z., Ma, Z., He, S., Fu, C., Wang, D., 2016a. Geochronological and Geochemical evidence of amphibolite from the Hualong Group, northwest China: Implication for the early Paleozoic accretionary tectonics of the Central Qilian belt. Lithos 248, 12-21.

Wang, W., Kirby, E., Peizhen, Z., Dewen, Z., Guangliang, Z., Huiping, Z., Wenjun, Z., Chizhang, C., 2013. Tertiary basin evolution along the northeastern margin of the Tibetan Plateau: Evidence for basin formation during Oligocene transtension. Geological Society of America Bulletin 125, 377-400.

Wang, W., Zhang, P., Pang, J., Garzione, C., Zhang, H., Liu, C., Zheng, D., Zheng, W., Yu, J., 2016b. The Cenozoic growth of the Qilian Shan in the northeastern Tibetan Plateau: A sedimentary archive from the Jiuxi Basin. Journal of Geophysical Research: Solid Earth 121, 2235-2257.

Wang, W., Zhang, P., Yu, J., Wang, Y., Zheng, D., Zheng, W., Zhang, H., Pang, J., 2016c. Constraints on mountain building in the northeastern Tibet: Detrital zircon records from synorogenic deposits in the Yumen Basin. Scientific Reports 6, 27604.

Wang, W., Zhang, P., Zheng, W., Zheng, D., Liu, C., Xu, H., Zhang, H., Yu, J., Pang, J., 2016d. Uplift-driven sediment redness decrease at~ 16.5 Ma in the Yumen Basin along the northeastern Tibetan Plateau. Scientific Reports 6.

Wang, W., Zheng, W., Zhang, P., Li, Q., Kirby, E., Yuan, D., Zheng, D., Liu, C., Wang, Z., Zhang, H., Pang, J., 2017c. Expansion of the Tibetan Plateau during the Neogene. 8, 15887.

Wang, X., Deng, L., Zattin, M., Ji, M., Li, J., 2017d. Palaeogene growth of the northeastern Tibetan Plateau: Detrital fission track and sedimentary analysis of the Lanzhou basin, NW China. Journal of Asian Earth Sciences 147, 322-331.

Wei, C., Song, S., 2008. Chloritoid–glaucophane schist in the north Qilian orogen, NW China: phase equilibria and P–T path from garnet zonation. Journal of Metamorphic Geology 26, 301-316.

Wittlinger, G., Tapponnier, P., Poupinet, G., Mei, J., Danian, S., Herquel, G., Masson, F., 1998. Tomographic evidence for localized lithospheric shear along the Altyn Tagh fault. Science 282, 74-76.

Wu, C., Yin, A., Zuza, A.V., Zhang, J., Liu, W., Ding, L., 2016. Pre-Cenozoic geologic history of the central and northern Tibetan Plateau and the role of Wilson cycles in constructing the Tethyan orogenic system. Lithosphere 8, 254-292.

Xia, X., Song, S., 2010. Forming age and tectono-petrogenises of the Jiugequan ophiolite in the North Qilian Mountain, NW China. Chinese Science Bulletin 55, 1899-1907.

Xiao, Q., Shao, G., Liu-Zeng, J., Oskin, M.E., Zhang, J., Zhao, G., Wang, J., 2015. Eastern termination of the Altyn Tagh Fault, western China: Constraints from a magnetotelluric survey. Journal of Geophysical Research: Solid Earth 120, 2838-2858.

Xiao, W., Mao, Q., Windley, B., Han, C., Qu, J., Zhang, J., Ao, S., Guo, Q., Cleven, N., Lin, S., 2010. Paleozoic multiple accretionary and collisional processes of the Beishan orogenic collage. American Journal of Science 310, 1553-1594.

Xu, G., Kamp, P.J., 2000. Tectonics and denudation adjacent to the Xianshuihe Fault, eastern Tibetan Plateau: Constraints from fission track thermochronology. Journal of Geophysical Research: Solid Earth 105, 19231-19251.

Xu, X., Song, S., Su, L., Li, Z., Niu, Y., Allen, M.B., 2015. The 600–580Ma continental rift basalts in North Qilian Shan, northwest China: Links between the Qilian-Qaidam block and SE Australia, and the reconstruction of East Gondwana. Precambrian Research 257, 47-64.

Xu, X., Wang, F., Zheng, R., Chen, W., Ma, W., Yu, G., Chen, G., Tapponnier, P., Van Der Woerd, J., Meriaux, A., 2005. Late Quaternary sinistral slip rate along the Altyn Tagh fault and its structural transformation model. Science in China Series D: Earth Sciences 48, 384-397.

Yang, J., Meng, F., Zhang, J., Li, H., 2001. The shoshonitic volcanic rocks at Hongliuxia: Pulses of the Altyn Tagh fault in Cretaceous? Science in China Series D: Earth Sciences 44, 94-102.

Yang, J.-H., Du, Y.-S., Cawood, P.A., Xu, Y.-J., 2009. Silurian collisional suturing onto the southern margin of the North China Craton: detrital zircon geochronology constraints from the Qilian Orogen. Sedimentary Geology 220, 95-104.

Yang, L., Zhu, L., Zheng, R., Yang, W., Wang, C., 2011. Sedimentary Characteristics and Tectonic Setting of the Lower Cretaceous strata in Jiuxi Basin, Gansu. Northwestern Geology 44, 112-118.

Yang, Z., Shen, C., Ratschbacher, L., Enkelmann, E., Jonckheere, R., Wauschkuhn, B., Dong, Y., 2017. Sichuan Basin and beyond: Eastward foreland growth of the Tibetan Plateau from an integration of Late Cretaceous-Cenozoic fission track and (U-Th)/He ages of the eastern Tibetan Plateau, Qinling, and Daba Shan. Journal of Geophysical Research: Solid Earth 122, 4712-4740.

Yin, A., Dang, Y.Q., Wang, L.C., Jiang, W.M., Zhou, S.P., Chen, X.H., Gehrels, G.E., McRivette, M.W., 2008. Cenozoic tectonic evolution of Qaidam basin and its surrounding

regions (Part 1): The southern Qilian Shan-Nan Shan thrust belt and northern Qaidam basin. Geological Society of America Bulletin 120, 813-846.

Yin, A., Harrison, T.M., 2000. Geologic evolution of the Himalayan-Tibetan orogen. Annual Review of Earth and Planetary Sciences 28, 211-280.

Yin, A., Rumelhart, P., Butler, R., Cowgill, E., Harrison, T., Foster, D., Ingersoll, R., Qing, Z., Xian-Qiang, Z., Xiao-Feng, W., 2002. Tectonic history of the Altyn Tagh fault system in northern Tibet inferred from Cenozoic sedimentation. Geological Society of America Bulletin 114, 1257-1295.

Yu, S., Zhang, J., Qin, H., Sun, D., Zhao, X., Cong, F., Li, Y., 2015. Petrogenesis of the early Paleozoic low-Mg and high-Mg adakitic rocks in the North Qilian orogenic belt, NW China: Implications for transition from crustal thickening to extension thinning. Journal of Asian Earth Sciences 107, 122-139.

Yuan, D.Y., Ge, W.P., Chen, Z.W., Li, C.Y., Wang, Z.C., Zhang, H.P., Zhang, P.Z., Zheng, D.W., Zheng, W.J., Craddock, W.H., 2013. The growth of northeastern Tibet and its relevance to large‐scale continental geodynamics: A review of recent studies. Tectonics 32, 1358-1370.

Yue, Y., Liou, J., 1999. Two-stage evolution model for the Altyn Tagh fault, China. Geology 27, 227-230.

Yue, Y., Ritts, B.D., Graham, S.A., Wooden, J.L., Gehrels, G.E., Zhang, Z., 2004a. Slowing extrusion tectonics: Lowered estimate of post-Early Miocene slip rate for the Altyn Tagh fault. Earth & Planetary Science Letters 217, 111–122.

Yue, Y.J., Ritts, B.D., Hanson, A.D., Graham, S.A., 2004b. Sedimentary evidence against large strike-slip translation on the Northern Altyn Tagh fault, NW China. Earth and Planetary Science Letters 228, 311-323.

Zeng, R., Lai, J., Mao, X., Li, B., Ju, P., Tao, S., 2016. Geochemistry, zircon U–Pb dating and Hf isotopies composition of Paleozoic granitoids in Jinchuan, NW China: Constraints on their petrogenesis, source characteristics and tectonic implication. Journal of Asian Earth Sciences 121, 20-33.

Zhang, B., Zhang, J., Wang, Y., Zhao, H., Li, Y., 2017. Late Mesozoic-Cenozoic Exhumation of the Northern Hexi Corridor: Constrained by Apatite Fission Track Ages of the Longshoushan. Acta Geologica Sinica - English Edition 91, 1624-1643.

Zhang, H.-p., Zhang, P.-z., Zheng, D.-W., Zheng, W.-J., Chen, Z.-W., Wang, W.-T., 2014. Transforming the Miocene Altyn Tagh fault slip into shortening of the north-western Qilian Shan: insights from the drainage basin geometry. Terra Nova 26, 216-221.

Zhang, J., Meng, F., Wan, Y., 2007a. A cold Early Palaeozoic subduction zone in the North Qilian Mountains, NW China: petrological and U - Pb geochronological constraints. Journal of Metamorphic Geology 25, 285-304.

Zhang, P.Z., Molnar, P., Xu, X.W., 2007b. Late Quaternary and present-day rates of slip along the Altyn Tagh Fault, northern margin of the Tibetan Plateau. Tectonics 26.

Zhao, Y., Sun, Y., Yan, J., Diwu, C., 2015. The Archean-Paleoproterozoic crustal evolution in the Dunhuang region, NW China: Constraints from zircon U–Pb geochronology and in situ Hf isotopes. Precambrian Research 271, 83-97.

Zheng, D., Clark, M.K., Zhang, P., Zheng, W., Farley, K.A., 2010. Erosion, fault initiation and topographic growth of the North Qilian Shan (northern Tibetan Plateau). Geosphere 6, 937-941.

Zheng, D., Wang, W., Wan, J., Yuan, D., Liu, C., Zheng, W., Zhang, H., Pang, J., Zhang, P., 2017a. Progressive northward growth of the northern Qilian Shan–Hexi Corridor (northeastern Tibet) during the Cenozoic. Lithosphere 9, 408-416.

Zheng, W., 2009. Geometric pattern and active tectonics of the Hexi Corridor and its adjacent regions. Institute of Geology, China Earthquake Administration, Beiing, Beijing, p. 140.

Zheng, W., Zhang, H.P., Zhang, P.Z., Molnar, P., Liu, X.W., Yuan, D.Y., 2013a. Late Quaternary slip rates of the thrust faults in western Hexi Corridor (Northern Qilian Shan, China) and their implications for northeastward growth of the Tibetan Plateau. Geosphere 9, 342-354.

Zheng, W., Zhang, P., He, W., Yuan, D., Shao, Y., Zheng, D., Ge, W.-p., Min, W., 2013b. Transformation of displacement between strike-slip and crustal shortening in the northern margin of the Tibetan Plateau: Evidence from decadal GPS measurements and late Quaternary slip rates on faults. Tectonophysics 584, 267-280.

Zheng, Y., Ding, Z., Cawood, P.A., Yue, S., 2017b. Geology, geochronology and isotopic geochemistry of the Xiaoliugou W–Mo ore field in the Qilian Orogen, NW China: Case study of a skarn system formed during continental collision. Ore Geology Reviews 81, 575-586.

Zhuang, G., Hourigan, J.K., Ritts, B.D., Kent-Corson, M.L., 2011. Cenozoic multiple-phase tectonic evolution of the northern Tibetan Plateau: Constraints from sedimentary records from Qaidam basin, Hexi Corridor, and Subei basin, northwest China. American Journal of Science 311, 116-152.

Zuza, A.V., Cheng, X., Yin, A., 2016. Testing models of Tibetan Plateau formation with Cenozoic shortening estimates across the Qilian Shan–Nan Shan thrust belt. Geosphere 12, 501-532.

Highlights

- Lower Cretaceous strata in the Yumen Basin derived from northern Qilian Shan and Bei Shan
- Contribution of the Qilian Shan source to the Yumen Basin largely increased during the Miocene
- The east segment of Altyn Tagh Fault terminates in the Yumen basin
- Our results highlight multiple stages of growth of the NE Tibetan plateau

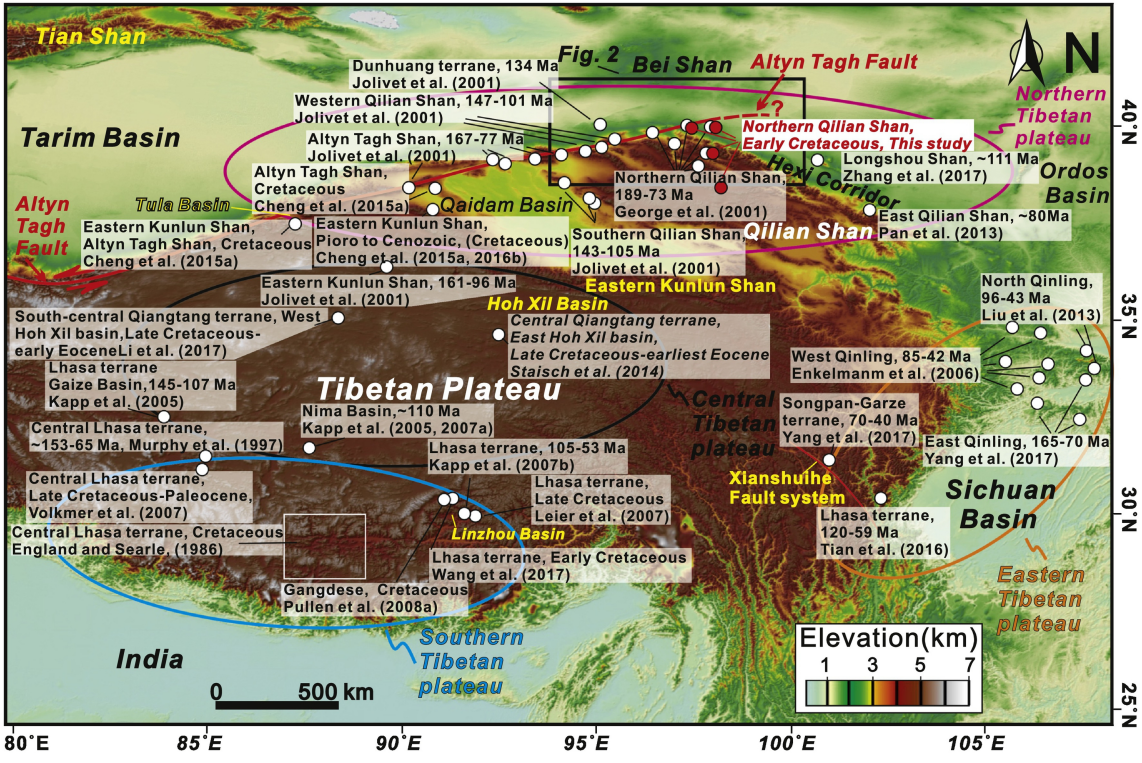
Tian Shan
Fig. 2
Bei Shan
Altyn Tagh Fault
N
Dunhuang terrane, 134 Ma
Jolivet et al. (2001)
Western Qilian Shan, 147-101 Ma
Jolivet et al. (2001)
Altyn Tagh Shan, 167-77 Ma
Jolivet et al. (2001)
Northern Qilian Shan,
Early Cretaceous, This study
Northern Tibetan plateau
Tarim Basin
Altyn Tagh Shan,
Cretaceous
Cheng et al. (2015a)
Northern Qilian Shan,
189-73 Ma
George et al. (2001)
Longshou Shan, ~111 Ma
Zhang et al. (2017)
Hexi Corridor
Ordos Basin
Altyn Tagh Fault
Tula Basin
Qaidam Basin
Eastern Kunlun Shan,
Altyn Tagh Shan, Cretaceous
Cheng et al. (2015a)
Eastern Kunlun Shan,
Pioro to Cenozoic, (Cretaceous)
Cheng et al. (2015a, 2016b)
Southern Qilian Shan
143-105 Ma
Jolivet et al. (2001)
Qilian Shan
East Qilian Shan, ~80Ma
Pan et al. (2013)
Eastern Kunlun Shan, 161-96 Ma
Jolivet et al. (2001)
Eastern Kunlun Shan
Hoh Xil Basin
North Qinling,
96-43 Ma
Liu et al. (2013)
South-central Qiangtang terrane, West
Hoh Xil basin,Late Cretaceous-
early EoceneLi et al. (2017)
Central Qiangtang terrane,
East Hoh Xil basin,
Late Cretaceous-earliest Eocene
Staisch et al. (2014)
West Qinling, 85-42 Ma
Enkelmanm et al. (2006)
Lhasa terrane
Gaize Basin,145-107 Ma
Kapp et al. (2005)
Tibetan Plateau
Central Tibetan plateau
Songpan-Garze
terrane, 70-40 Ma
Yang et al. (2017)
East Qinling, 165-70 Ma
Yang et al. (2017)
Nima Basin,~110 Ma
Kapp et al. (2005, 2007a)
Central Lhasa terrane,
~153-65 Ma, Murphy et al. (1997)
Lhasa terrane, 105-53 Ma
Kapp et al. (2007b)
Xianshuihe
Fault system
Sichuan Basin
Central Lhasa terrane,
Late Cretaceous-Paleocene,
Volkmer et al. (2007)
Lhasa terrane,
Late Cretaceous
Leier et al. (2007)
Lhasa terrane,
120-59 Ma
Tian et al. (2016)
Linzhou Basin
Central Lhasa terrane, Cretaceous
England and Searle, (1986)
Lhasa terrane, Early Cretaceous
Wang et al. (2017)
Eastern Tibetan plateau
Gangdese, Cretaceous
Pullen et al. (2008a)
Southern Tibetan plateau
India
Elevation(km)
1 3 5 7
0 500 km
40˚N
35˚N
30˚N
25˚N
80˚E
85˚E
90˚E
95˚E
100˚E
105˚E

Figure 1

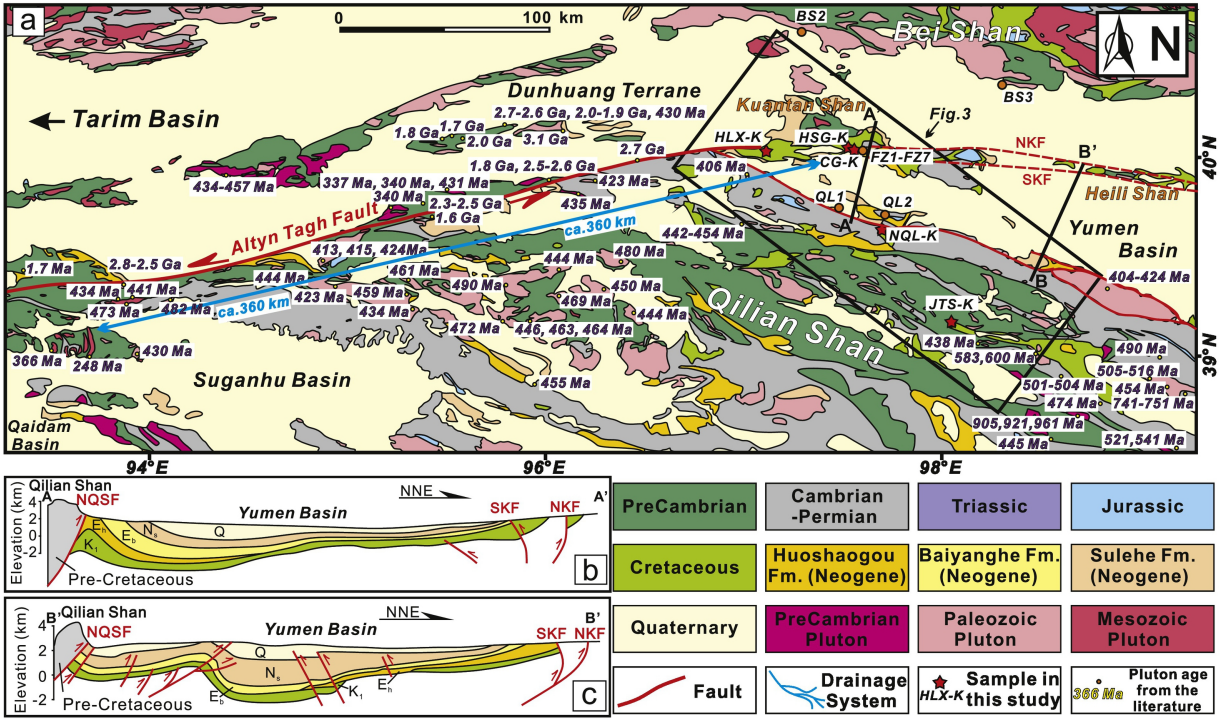
a
0
100 km
N
BS2
Bei Shan
BS3
Dunhuang Terrane
Kuantan Shan
Tarim Basin
Fig.3
HLX-K
HSG-K
CG-K
FZ1-FZ7
NKF
SKF
B'
A
A'
Heili Shan
Yumen Basin
QL1
QL2
NQL-K
Altyn Tagh Fault
ca.360 km
Qilian Shan
Suganhu Basin
Qaidam Basin
JTS-K
40°N
39°N
94°E
96°E
98°E
b
c
Elevation (km)
NQSF
NNE
SKF
NKF
Pre-Cretaceous
PreCambrian
Cambrian -Permian
Triassic
Jurassic
Cretaceous
Huoshaogou Fm. (Neogene)
Baiyanghe Fm. (Neogene)
Sulehe Fm. (Neogene)
Quaternary
PreCambrian Pluton
Paleozoic Pluton
Mesozoic Pluton
Fault
Drainage System
Sample in this study
Pluton age from the literature

Figure 2

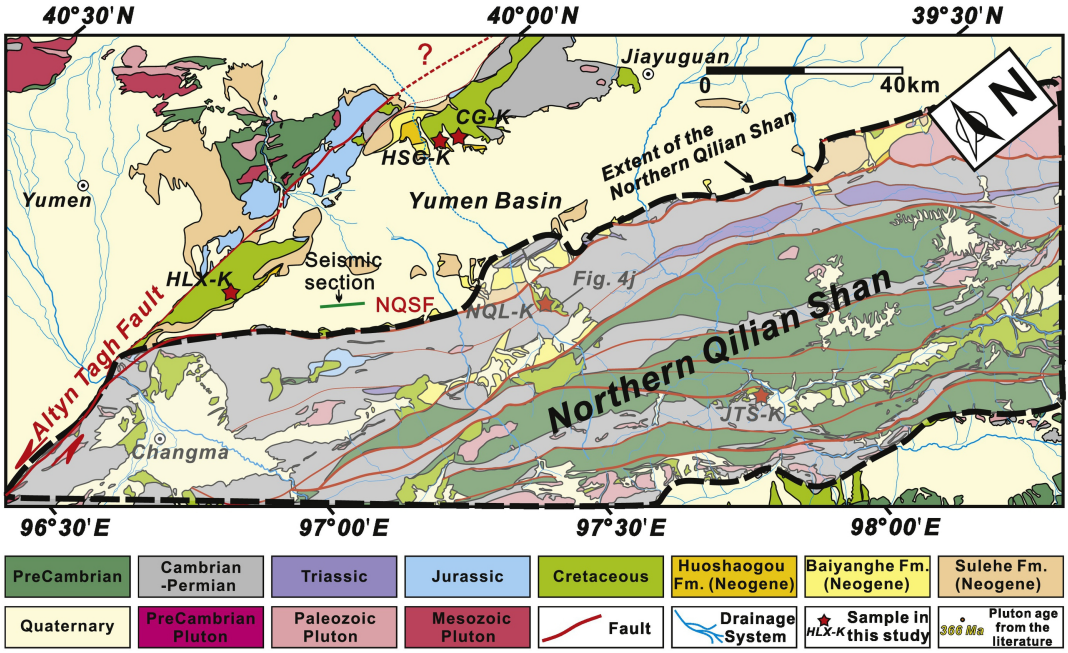
40°30'N
40°00'N
39°30'N
96°30'E
97°00'E
97°30'E
98°00'E
Jiayuguan
0
40km
N
Extent of the Northern Qilian Shan
CG-K
HSG-K
Yumen
Yumen Basin
Seismic section
NQSF
HLX-K
NQL-K
Fig. 4j
Altyn Tagh Fault
Northern Qilian Shan
JTS-K
Changma
PreCambrian
Cambrian -Permian
Triassic
Jurassic
Cretaceous
Huoshaogou Fm. (Neogene)
Baiyanghe Fm. (Neogene)
Sulehe Fm. (Neogene)
Quaternary
PreCambrian Pluton
Paleozoic Pluton
Mesozoic Pluton
Fault
Drainage System
HLX-K Sample in this study
366 Ma Pluton age from the literature

Figure 3

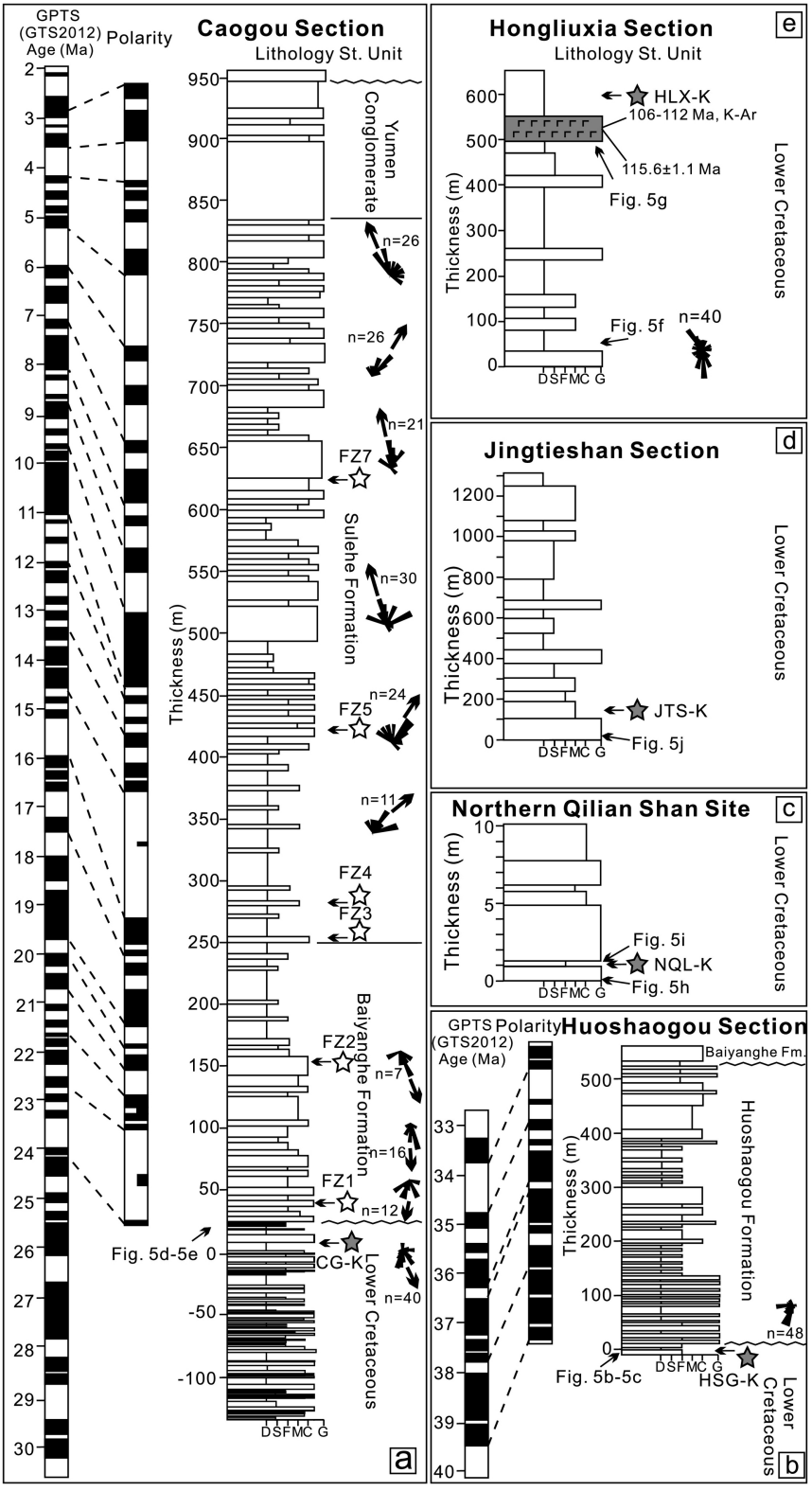
GPTS (GTS2012) Age (Ma)
Polarity
Caogou Section
Lithology St. Unit
Thickness (m)
Yumen Conglomerate
Suiehe Formation
Baiyanghe Formation
Lower Cretaceous
n=26
n=26
n=21
n=30
n=24
n=11
n=7
n=16
n=12
n=40
FZ7
FZ5
FZ4
FZ3
FZ2
FZ1
CG-K
Fig. 5d-5e
D S F M C G
a
Hongliuxia Section
e
HLX-K
106-112 Ma, K-Ar
115.6±1.1 Ma
Fig. 5g
Fig. 5f
n=40
Jingtieshan Section
d
JTS-K
Fig. 5j
Northern Qilian Shan Site
c
Fig. 5i
NQL-K
Fig. 5h
Huoshaogou Section
Baiyanghe Fm.
Huoshaogou Formation
n=48
Fig. 5b-5c
HSG-K
b

Figure 4


East
a
Ordovician rocks
Normal fault
Coarse grained sedimentary rocks
150°∠26°
Cretaceous strata
fine grained sedimentary rocks
Unconformity
Ordovician rocks
Unconformity
Unconformity
Quaternary sediments
Inferred fault plane
Dip to the east
b
Jiuquan Conglomerate
Eocene Huoshaogou Fm.
165°∠20°
145°∠16°
Lower Cretaceous strata
Huoshaogou Section
c
Lower Cretaceous mudstone
Huoshaogou Section
d
Jiuquan Conglomerate
116°∠26°
Lower Cretaceous strata
Oligocene
Baiyanghe Fm.
Caogou Section
e
Braided river deposit in the
Lower Cretaceous strata
Caogou Section
f
Oligocene
Baiyanghe Fm.
215°∠49°
Lower Cretaceous strata
Hongliuxia Section
g
Basalt
(106-112 Ma, K-Ar age)
(115.6 ± 1.1 Ma, U-Pb age)
220°∠45°
Lower
Cretaceous
strata
Hongliuxia Section
h
260°∠30°
Thick bedded conglomerate
Northern Qilian Section
50 cm
i
Sandstone intercalation
Northern Qilian Section
j
240°∠12°
Thick bedded conglomerate
Jingtieshan Section

Figure 5

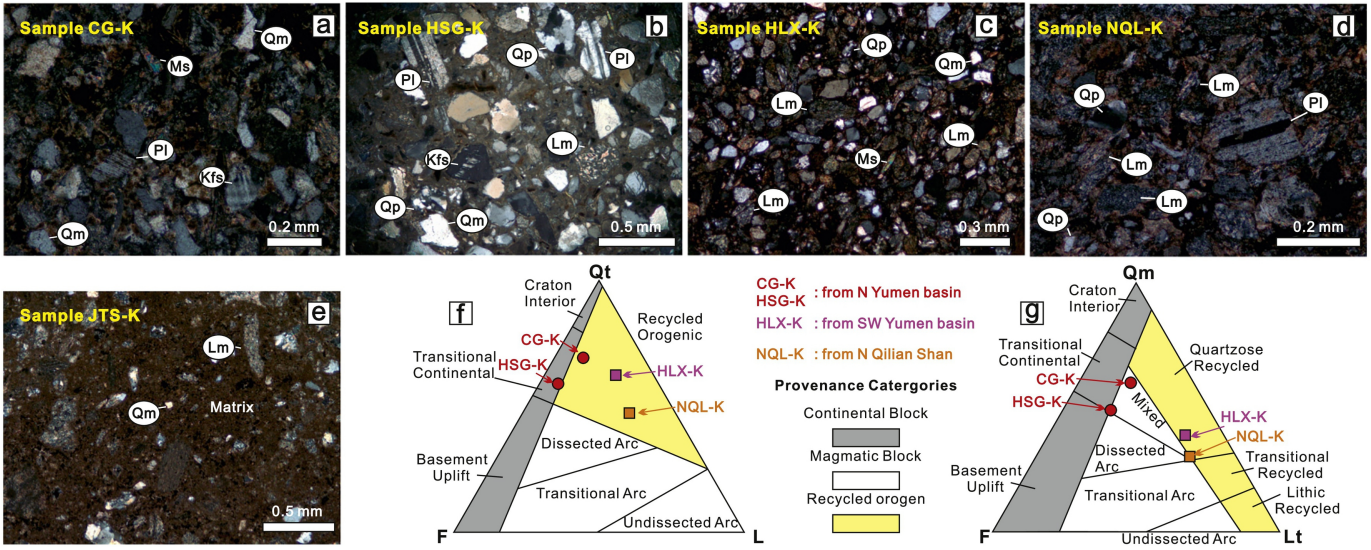
Sample CG-K
a
Qm
Ms
Pl
Kfs
Qm
0.2 mm
Sample HSG-K
b
Pl
Qp
Pl
Lm
Kfs
Qp
Qm
0.5 mm
Sample HLX-K
c
Qp
Qm
Lm
Lm
Ms
Lm
0.3 mm
Sample NQL-K
d
Qp
Lm
Pl
Lm
Lm
Qp
0.2 mm
Sample JTS-K
e
Lm
Qm
Matrix
0.5 mm
f
Qt
Craton Interior
Recycled Orogenic
Transitional Continental
CG-K
HSG-K
HLX-K
NQL-K
Basement Uplift
Dissected Arc
Transitional Arc
Undissected Arc
F
L
CG-K
HSG-K : from N Yumen basin
HLX-K : from SW Yumen basin
NQL-K : from N Qilian Shan
Provenance Catergories
Continental Block
Magmatic Block
Recycled orogen
g
Qm
Craton Interior
Transitional Continental
Quartzose Recycled
CG-K
HSG-K
Mixed
HLX-K
NQL-K
Basement Uplift
Dissected Arc
Transitional Recycled
Transitional Arc
Lithic Recycled
Undissected Arc
F
Lt

Figure 6

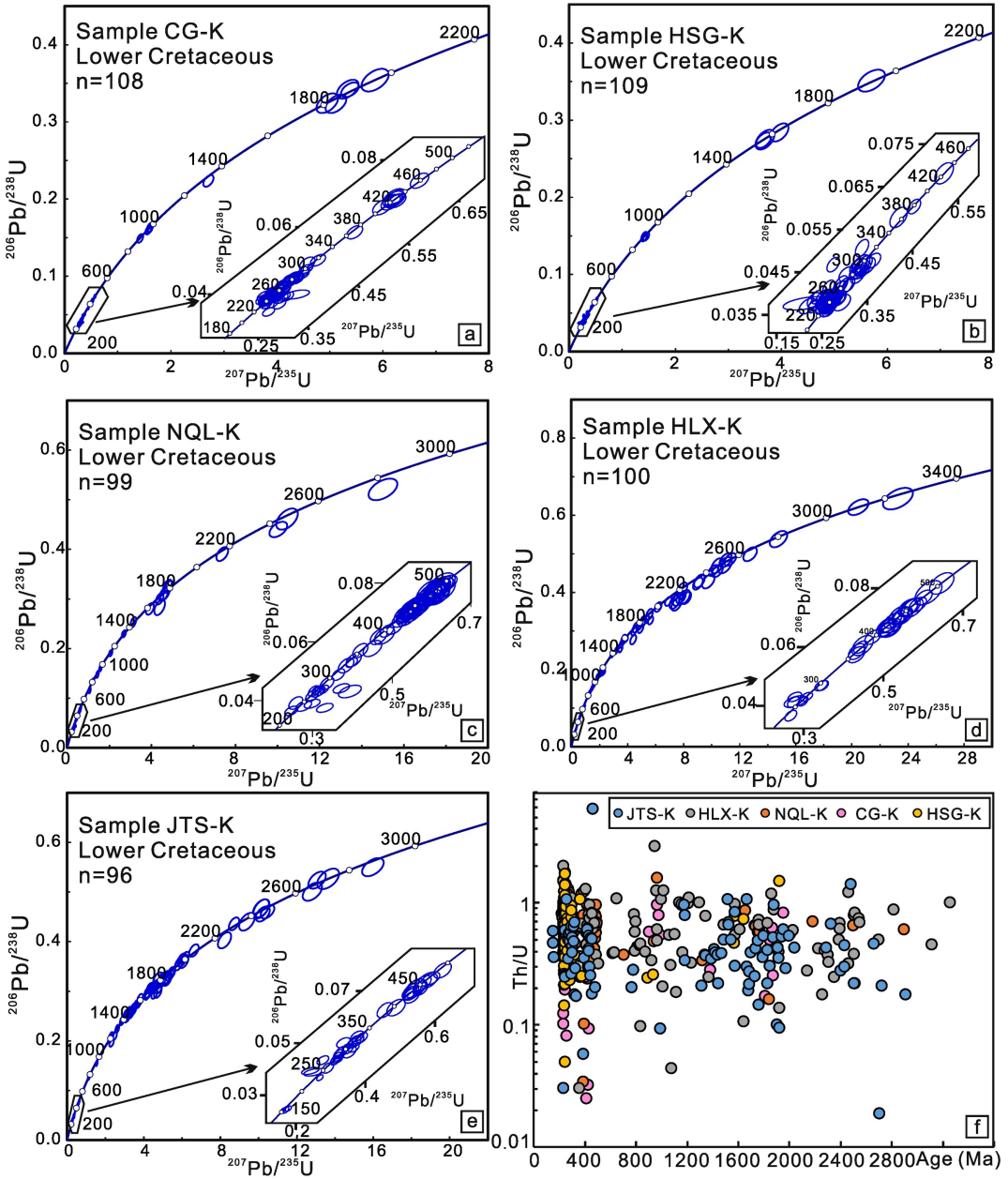
Sample CG-K
Lower Cretaceous
n=108
a
Sample HSG-K
Lower Cretaceous
n=109
b
Sample NQL-K
Lower Cretaceous
n=99
c
Sample HLX-K
Lower Cretaceous
n=100
d
Sample JTS-K
Lower Cretaceous
n=96
e
JTS-K HLX-K NQL-K CG-K HSG-K
f
$^{206}Pb/^{238}U$
$^{207}Pb/^{235}U$
Th/U
Age (Ma)

Figure 7

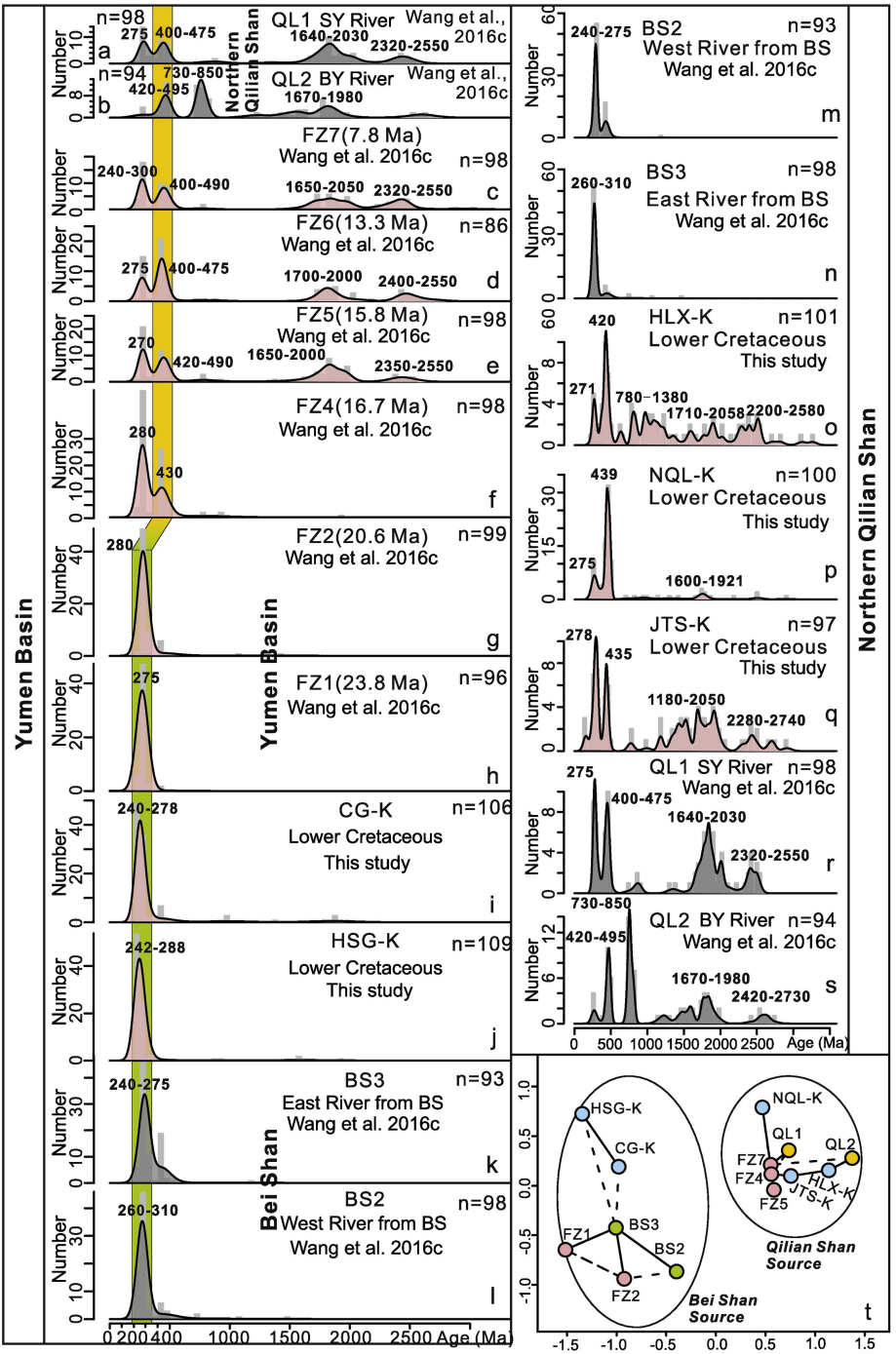
Yumen Basin
Bei Shan
Northern Qilian Shan
n=98
275 400-475
1640-2030
2320-2550
QL1 SY River Wang et al., 2016c
a
n=94
730-850
420-495
1670-1980
QL2 BY River Wang et al., 2016c
b
FZ7(7.8 Ma)
Wang et al. 2016c
n=98
240-300
400-490
1650-2050
2320-2550
c
FZ6(13.3 Ma)
Wang et al. 2016c
n=86
275
400-475
1700-2000
2400-2550
d
FZ5(15.8 Ma)
Wang et al. 2016c
n=98
270
420-490
1650-2000
2350-2550
e
FZ4(16.7 Ma)
Wang et al. 2016c
n=98
280
430
f
FZ2(20.6 Ma)
Wang et al. 2016c
n=99
280
g
FZ1(23.8 Ma)
Wang et al. 2016c
n=96
275
h
CG-K
Lower Cretaceous
This study
n=106
240-278
i
HSG-K
Lower Cretaceous
This study
n=109
242-288
j
BS3
East River from BS
Wang et al. 2016c
n=93
240-275
k
BS2
West River from BS
Wang et al. 2016c
n=98
260-310
l
Number
0 200 400 1000 1500 2000 2500 Age (Ma)
BS2
West River from BS
Wang et al. 2016c
n=93
240-275
m
BS3
East River from BS
Wang et al. 2016c
n=98
260-310
n
HLX-K
Lower Cretaceous
This study
n=101
420
271
780-1380
1710-2058
2200-2580
o
NQL-K
Lower Cretaceous
This study
n=100
439
275
1600-1921
p
JTS-K
Lower Cretaceous
This study
n=97
278
435
1180-2050
2280-2740
q
QL1 SY River
Wang et al. 2016c
n=98
275
400-475
1640-2030
2320-2550
r
QL2 BY River
Wang et al. 2016c
n=94
730-850
420-495
1670-1980
2420-2730
s
0 500 1000 1500 2000 2500 Age (Ma)
HSG-K
CG-K
BS3
FZ1
BS2
FZ2
Bei Shan Source
NQL-K
QL1
QL2
FZ7
FZ4
FZ5
HLX-K
JTS-K
Qilian Shan Source
t

Figure 8

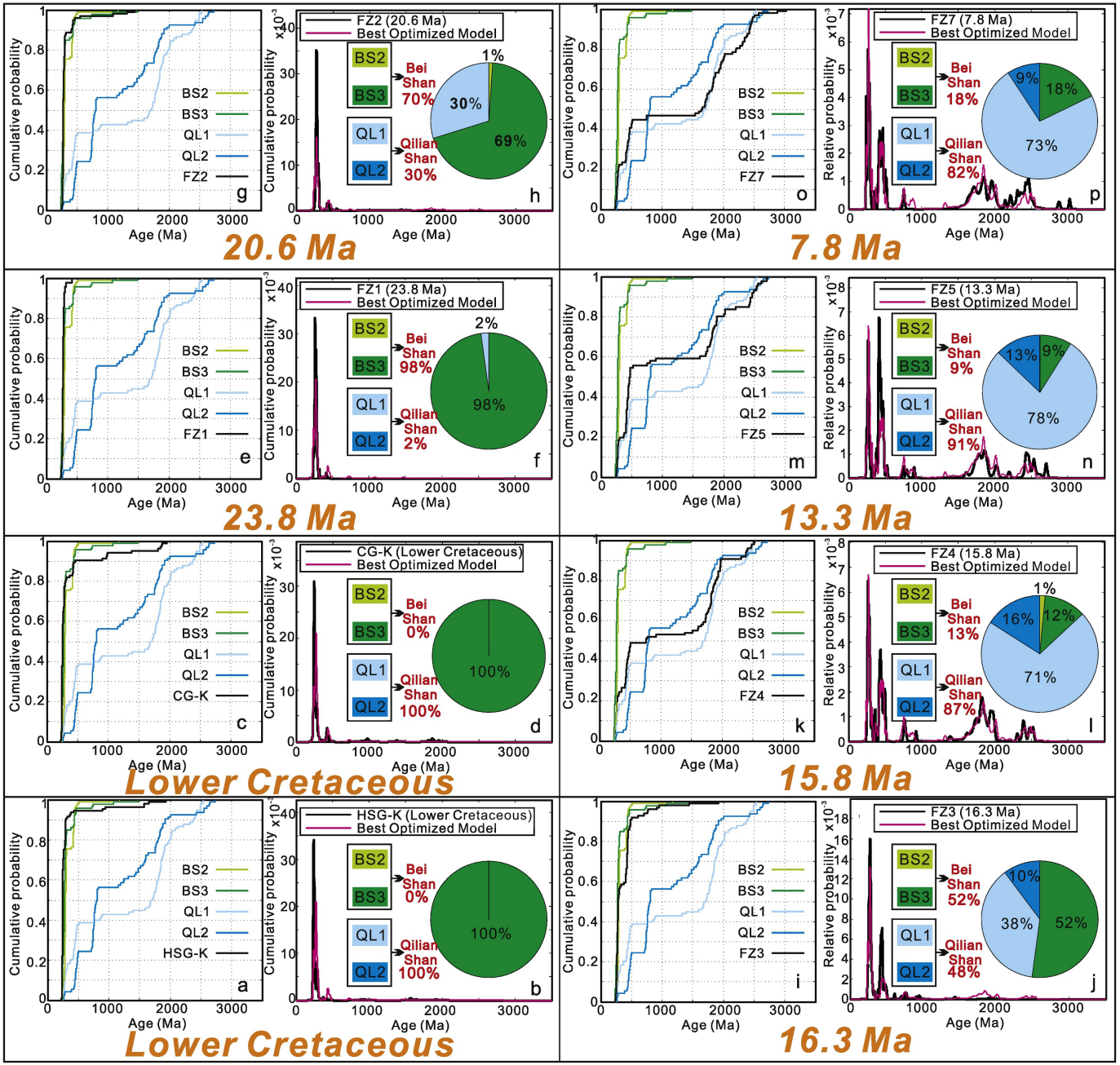
20.6 Ma
7.8 Ma
23.8 Ma
13.3 Ma
Lower Cretaceous
15.8 Ma
Lower Cretaceous
16.3 Ma
Cumulative probability
Relative probability
Age (Ma)
BS2
BS3
QL1
QL2
FZ2
FZ7
FZ1
FZ5
CG-K
FZ4
HSG-K
FZ3
FZ2 (20.6 Ma)
FZ7 (7.8 Ma)
FZ1 (23.8 Ma)
FZ5 (13.3 Ma)
CG-K (Lower Cretaceous)
FZ4 (15.8 Ma)
HSG-K (Lower Cretaceous)
FZ3 (16.3 Ma)
Best Optimized Model
Bei Shan 70%
Qilian Shan 30%
Bei Shan 18%
Qilian Shan 82%
Bei Shan 98%
Qilian Shan 2%
Bei Shan 9%
Qilian Shan 91%
Bei Shan 0%
Qilian Shan 100%
Bei Shan 13%
Qilian Shan 87%
Bei Shan 0%
Qilian Shan 100%
Bei Shan 52%
Qilian Shan 48%
1%
30%
69%
9%
18%
73%
2%
98%
13%
9%
78%
1%
16%
12%
71%
10%
38%
52%
a
b
c
d
e
f
g
h
i
j
k
l
m
n
o
p

Figure 9

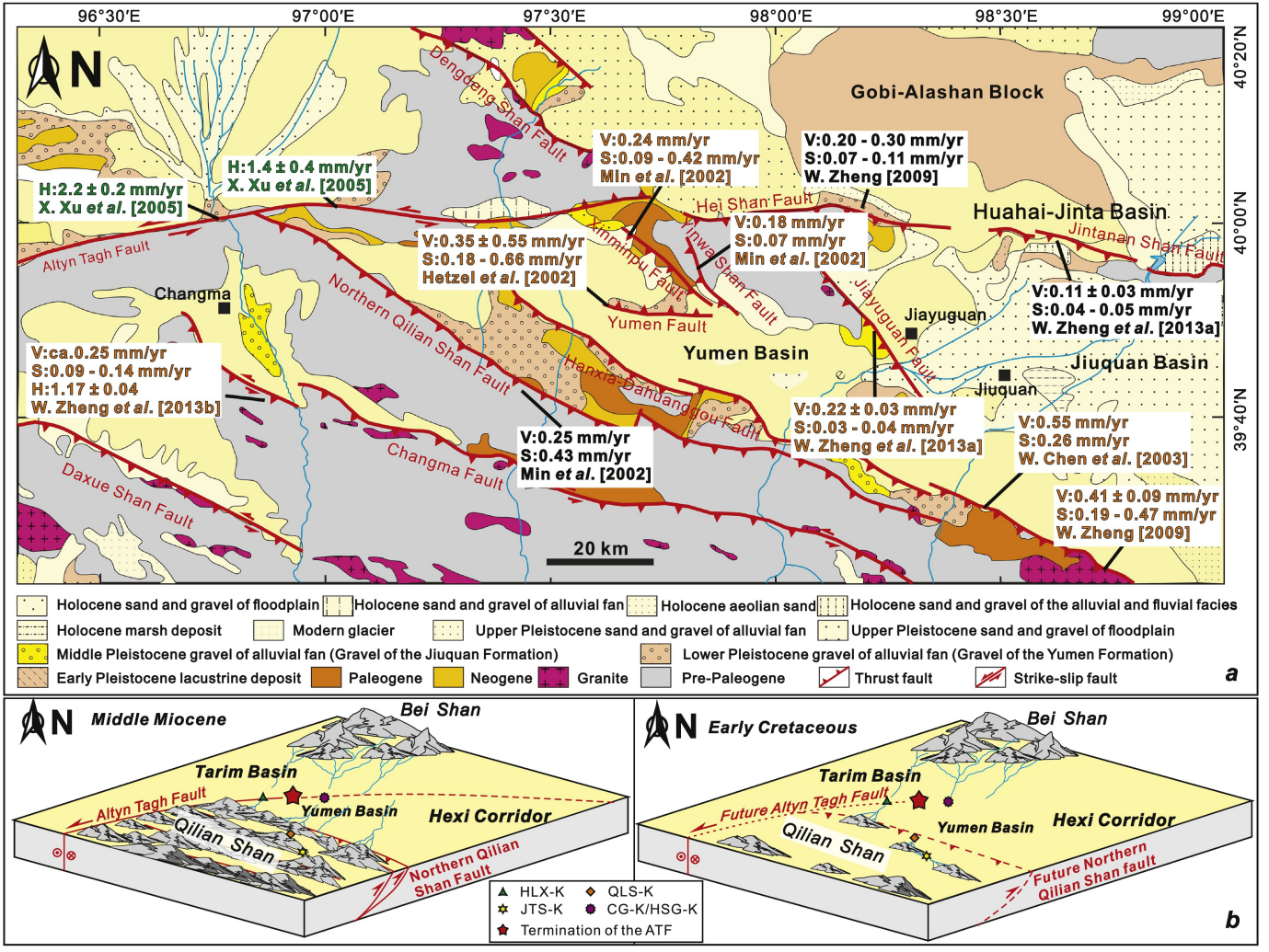
96°30'E
97°00'E
97°30'E
98°00'E
98°30'E
99°00'E
40°20'N
40°00'N
39°40'N
N
Gobi-Alashan Block
Huahai-Jinta Basin
Jiuquan Basin
Yumen Basin
Changma
Jiayuguan
Jiuquan
Dengdeng Shan Fault
Hei Shan Fault
Jintanan Shan Fault
Altyn Tagh Fault
Ximimpu Fault
Yinwa Shan Fault
Jiayuguan Fault
Yumen Fault
Northern Qilian Shan Fault
Hanxia-Damaguan Fault
Changma Fault
Daxue Shan Fault
H:2.2 ± 0.2 mm/yr
X. Xu et al. [2005]
H:1.4 ± 0.4 mm/yr
X. Xu et al. [2005]
V:0.24 mm/yr
S:0.09 - 0.42 mm/yr
Min et al. [2002]
V:0.20 - 0.30 mm/yr
S:0.07 - 0.11 mm/yr
W. Zheng [2009]
V:0.35 ± 0.55 mm/yr
S:0.18 - 0.66 mm/yr
Hetzel et al. [2002]
V:0.18 mm/yr
S:0.07 mm/yr
Min et al. [2002]
V:0.11 ± 0.03 mm/yr
S:0.04 - 0.05 mm/yr
W. Zheng et al. [2013a]
V:ca.0.25 mm/yr
S:0.09 - 0.14 mm/yr
H:1.17 ± 0.04
W. Zheng et al. [2013b]
V:0.25 mm/yr
S:0.43 mm/yr
Min et al. [2002]
V:0.22 ± 0.03 mm/yr
S:0.03 - 0.04 mm/yr
W. Zheng et al. [2013a]
V:0.55 mm/yr
S:0.26 mm/yr
W. Chen et al. [2003]
V:0.41 ± 0.09 mm/yr
S:0.19 - 0.47 mm/yr
W. Zheng [2009]
20 km
Holocene sand and gravel of floodplain
Holocene sand and gravel of alluvial fan
Holocene aeolian sand
Holocene sand and gravel of the alluvial and fluvial facies
Holocene marsh deposit
Modern glacier
Upper Pleistocene sand and gravel of alluvial fan
Upper Pleistocene sand and gravel of floodplain
Middle Pleistocene gravel of alluvial fan (Gravel of the Jiuquan Formation)
Lower Pleistocene gravel of alluvial fan (Gravel of the Yumen Formation)
Early Pleistocene lacustrine deposit
Paleogene
Neogene
Granite
Pre-Paleogene
Thrust fault
Strike-slip fault
a
N
Middle Miocene
Bei Shan
Tarim Basin
Altyn Tagh Fault
Yumen Basin
Hexi Corridor
Qilian Shan
Northern Qilian Shan Fault
HLX-K
QLS-K
JTS-K
CG-K/HSG-K
Termination of the ATF
N
Early Cretaceous
Bei Shan
Tarim Basin
Future Altyn Tagh Fault
Yumen Basin
Hexi Corridor
Qilian Shan
Future Northern Qilian Shan fault
b

Figure 10